

Pipeline quantum processor architecture for silicon spin qubits

S. M. Patomäki,^{1,2} M. F. Gonzalez-Zalba,¹ M. A. Fogarty,¹ Z. Cai,^{3,1} S. C. Benjamin,^{1,3} and J. J. L. Morton^{1,2}

¹ *Quantum Motion, 9 Sterling Way, London N7 9HJ, United Kingdom*

² *London Centre for Nanotechnology, University College London, London WC1H 0AH, United Kingdom**

³ *Department of Materials, University of Oxford, Parks Road, Oxford OX1 3PH, United Kingdom*

(Dated: June 14, 2023)

Noisy intermediate-scale quantum (NISQ) devices seek to achieve quantum advantage over classical systems without the use of full quantum error correction. We propose a NISQ processor architecture using a qubit ‘pipeline’ in which all run-time control is applied globally, reducing the required number and complexity of control and interconnect resources. This is achieved by progressing qubit states through a layered physical array of structures which realise single and two-qubit gates. Such an approach lends itself to NISQ applications such as variational quantum eigensolvers which require numerous repetitions of the same calculation, or small variations thereof. In exchange for simplifying run-time control, a larger number of physical structures is required for shuttling the qubits as the circuit depth now corresponds to an array of physical structures. However, qubit states can be ‘pipelined’ densely through the arrays for repeated runs to make more efficient use of physical resources. We describe how the qubit pipeline can be implemented in a silicon spin-qubit platform, to which it is well suited to due to the high qubit density and scalability. In this implementation, we describe the physical realisation of single and two qubit gates which represent a universal gate set that can achieve fidelities of $\mathcal{F} \geq 0.9999$, even under typical qubit frequency variations.

I. INTRODUCTION

Fault-tolerant quantum computers offer profound computational speed-ups across diverse applications, but are challenging to build. However, even in the near term without full error correction, quantum computers have the potential to offer improvements over classical computing approaches in run time scaling [1] and energy consumption for certain tasks [2]. There is a rich and diverse array of schemes for realising quantum computation, each formally equivalent in computational power [3–5], with important differences with regards to practical realisations. In the gate-based approach, a quantum algorithm is expressed as a quantum circuit consisting of a series of quantum logic gates. Typically, such gates are applied to a stationary array of qubits (for example through electromagnetic waves or optical pulses), relying on the delivery of a complex series of accurate, quasi-simultaneous control pulses to each qubit. This can lead to practical challenges ranging from cross-talk in the control pulses between nearby qubits [6, 7] to increased demands on digital-to-analogue converters (DACs) particularly when fully integrating control systems with a cryogenic quantum chip.

To mitigate the practical challenges associated with high-density control electronics, global qubit control schemes have been explored [8–10]. However, these approaches require a precision in the position and homogeneity of qubit structures, as well as the control pulses, to a degree that is technically challenging with available technology. Alternatively, local addressing can be used to bring qubits into resonance with globally applied control

fields to create an effective local control [11, 12]. However, this approach still requires fast run-time control for the addressing [13]. A second strategy is to accept the cost of a much lower effective qubit density in exchange for mitigating effects such as cross-talk — in such a distributed model of quantum computing [14] qubits, or small qubit registers, are well-separated and interfaced by a common entangling (typically photonic) mode. While such hybrid matter/photon systems have been successfully realised in several platforms [15–17], high gate speeds compatible with the demands of NISQ algorithms [18] may be difficult to achieve.

A further consideration when designing NISQ hardware architectures is that NISQ algorithms based on (e.g.) variational approaches [18, 19] require multiple repetitions of the same quantum circuit — or simple variations thereof — to be performed. In turn this requires identical, or similar, sequences of local control fields to be repetitively applied to the qubits, presenting an opportunity for more efficient hardware implementations. In this Article, we propose a quantum computing architecture for implementing quantum circuits in which all runtime control is applied globally, and local quantum operations such as 1-qubit (1Q) and 2-qubit (2Q) gates are ‘programmed’ into the array in advance. This is achieved by shuttling qubit states through a grid of gated structures which have been electronically configured to realise specific gates.

In such an approach, each layer of gates in the original quantum circuit corresponds to a one-dimensional array of structures, such that the scheme is more demanding in terms of physical resources on a chip for confining qubits. However, when applying multiple repetitions of the same circuit by *pipelining* — i.e. running distinct, staggered layers of qubits through the array simultaneously — the physical resource efficiency becomes broadly equivalent

* ucapsmp@ucl.ac.uk

to more conventional approaches, combined with potential practical benefits.

Below, we introduce the concept of a qubit pipeline in more detail in Sec. II, before focusing on a potential implementation for the silicon metal-oxide-semiconductor (SiMOS) electron spin qubit platform in Sec. III. We then estimate the expected improvement in run time for an example algorithm in Sec. IV. In particular, in Sec. III A, we outline a scheme for synchronous shuttling, and in Sec. III B, we discuss initialisation, readout, and parallelised pre-configuration, mostly outlining established methods. In Sections III C-III E, we show how to realise an universal gate set for the pipeline in the silicon electron spin platform including: single-qubit Z -rotations using local, voltage-controllable g -factor Stark shifts, globally-applied \sqrt{X} operations enabled by B_1 -drive frequency binning and 2Q SWAP-rotation gates using the native interaction of nearest neighbour exchange. Each of the above gate implementations is designed to accommodate natural variations, such as random g -factor differences, across the QDs while enabling synchronized operation and thus fixed gate times.

II. QUBIT PIPELINE

For solid-state quantum processors the qubit array may consist of a two-dimensional lattice with nearest-neighbour couplings (see Fig. 1(a)). The qubit pipeline approach replaces the two-dimensional lattice of stationary qubits with an $N \times D$ grid (see Fig. 1(b)), such that N qubits are arranged in a one-dimensional array and propagate through the grid to perform a quantum circuit of depth D . Each column therefore represents a single ‘time step’ of quantum logic gates in the corresponding quantum circuit while each row of structures forms a ‘pipe’ of computational length D along which a qubit travels. Multiple qubits can simultaneously travel through each pipe, at different stages, in order to more efficiently use the physical resource.

Run-time operation begins by initializing a one-dimensional array of N qubit states on the input edge. This initialised array is synchronously pushed through D structures that have been preconfigured to perform the single- and two-qubit gates in the desired quantum circuit. Qubit states are read out on the opposite output edge. Between initialization and readout, operations on the qubit array alternate between synchronous one- and two-qubit gate steps and shuttling steps. Figures 1 (c)-(f) illustrate the equivalence between an example quantum circuit (Fig. 1 (c)) and time-evolution on the qubit pipeline (Figs. 1 (d)-(f)). In this way, local qubit control of the typical qubit grid is replaced by a combination of global control (at least, with widely shared control lines) to push the qubit states from start to finish, combined with quasi-statically tuneable elements within the larger number of physical structures used to define the quantum circuit prior to running it.

We assume that while the parameters of the quantum logic gates can be tuned in-situ (e.g. electrically), the type of gate performed in each cell of the array is defined when fabricating the quantum processor. Indeed, though more generally reconfigurable implementations may be possible (see e.g. Supplementary Sec. S1) and offer potential efficiencies, a suitably chosen pattern of gates is sufficient for universal quantum computation, subject only to the constraints of the qubit number and circuit depth. Assuming the quantum processor is restricted to a two-dimensional topology, the pipeline approach presented here is limited to a linear qubit array. Many quantum algorithms can be mapped onto such a linear array without significant loss of efficiency, such as the variational quantum eigensolver for the Fermi-Hubbard model, a promising task that could be implemented on NISQ hardware [18–21].

Conventional approaches to operate an N qubit processor with tuneable nearest neighbour couplings demand at least $\mathcal{O}(N)$ fast signal generators for single-qubit control, for qubit-qubit couplings, and for state readout. In contrast, the pipeline scheme presented here may require a constant (even just one) number of fast pulse generators, utilized for shuttling the qubit states through the grid in a manner analogous to a charge-coupled device. For example, three waveforms biasing columns $d \bmod 3 = 0$, $d \bmod 3 = 1$, and $d \bmod 3 = 2$, create a local potential minimum for a qubit which can then be driven forward through the array [22]. Implementing such a shuttling scheme, synchronicity is achieved if gate steps take an equal amount of time for all qubits. For example, for logic gates expressed as $\exp(-i\omega\tau\sigma)$ for some single- or two-qubit operator σ , we fix a common τ but select ω to control the amount of rotation and thus distinguish the logic operations. The gate speed ω is varied using parameters such as dc gate voltages and magnetic field amplitudes at the preconfiguration stage. In principle, different columns of gates (e.g. all single-qubit gates, or all two-qubit gates) could have different durations, at the cost of a more complex shuttling pulse sequence. The three-column approach to shuttling represents the maximum density with which different sets of qubits can be pipelined through the circuit.

Due to the statistical nature of measurement in quantum mechanics, several types of quantum algorithms, such as those that yield an expectation value following some quantum circuit [23, 24], must be run a large number of times to obtain a meaningful result. Such algorithms are well-suited to the pipeline approach as multiple, independent qubit arrays can be pushed through the pipeline simultaneously, enabling multiple circuit runs in parallel. The maximum density of independent logical instances of a quantum circuit which can be pipelined through the structure is determined by the physical constraints of ensuring forward shuttling and avoiding unwanted interactions between qubits. Furthermore, if the duration of either the initialisation or readout stage is greater than that of the 1Q/2Q gates, this density must

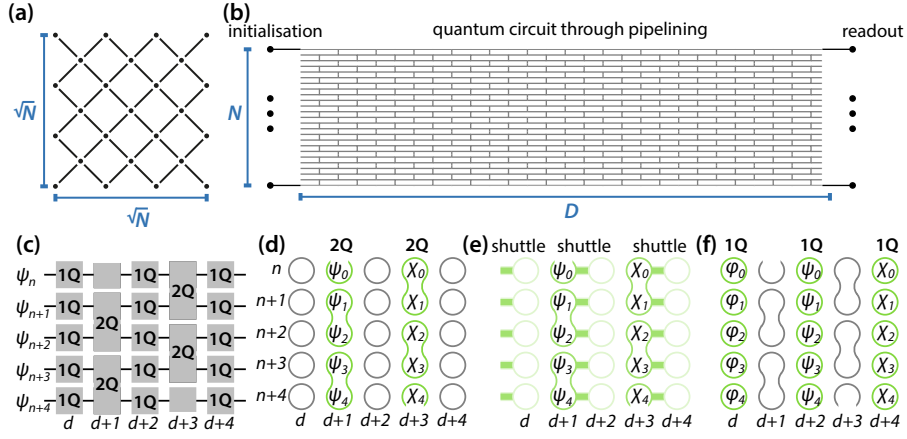


Figure 1. **The qubit pipeline.** (a) In a typical N -qubit solid state quantum processor, qubits reside at fixed spatial locations (e.g. on a $\sqrt{N} \times \sqrt{N}$ grid) with nearest-neighbour connectivity. (b) The qubit pipeline is a weaved grid in which N qubits are shuttled through D locations where fixed single- (1Q) or two-qubit (2Q) logic gates are implemented. Vertical lines indicate 2Q couplers, while horizontal lines indicate shuttling couplers. At runtime, qubits are initialized at one end, synchronously shuttled through the pipeline, and read out on the opposite end. (c) An example quantum circuit diagram, where an algorithm is decomposed into alternating steps of 1Q and 2Q gates. (d)-(f) The qubit pipeline contains physical locations which have been configured to implement 1Q (circles) and 2Q (connected circles) gates. Different qubit arrays (first (χ_0, χ_1, \dots) , then (ψ_0, ψ_1, \dots) , $(\varphi_0, \varphi_1, \dots)$) can be piped sequentially through the structures, each representing one execution of the configured quantum circuit.

	Lattice	Pipeline
Processor size	$\sqrt{N} \times \sqrt{N}$	$N \times D$
Run-time control resources	N	constant
Circuit decomposition	flexible	limited
Runtime scaling	DN_r	$D + N_r$

Table I. **Comparison between the quantum lattice and the pipeline processors.** Here, N is the number of qubits, D is the maximum circuit depth, and N_r is the number of repetitions.

be further reduced. Exploiting such pipelining, the algorithm runtime is proportional to $(D + N_r)\tau$ instead of $DN_r\tau$, providing a significant speedup for circuits with large number of repetitions N_r , or large depths. Here, τ is the timescale of the longest operation: a qubit gate, readout, or initialization. Table I summarises these main differences between a qubit lattice and the qubit pipeline.

III. IMPLEMENTATION WITH SILICON QUANTUM DOTS

We now analyse a hardware implementation well-suited to the qubit pipeline paradigm, i.e. qubits based on single electron spins trapped in silicon-based QDs. Silicon spin qubits can achieve high density due to their

small footprint of $\mathcal{O}(50 \times 50 \text{ nm}^2)$, and can leverage the state-of-the-art nanoscale complementary metal-oxide-semiconductor (CMOS) manufacturing technology used in microprocessors [7, 25–27]. Quasi-CMOS-compatible electron spin qubits can be patterned as gated planar MOS devices [28–30], confining electrons at the Si-SiO₂ interface below the gates, or using Si/SiGe heterostructures [30, 31]. Typical values for single- and two-qubit gate fidelities measured so far in such systems include 99.96% and 99.48% in SiMOS [32, 33] and 99.9% and 99.5% in Si/SiGe [31, 34, 35]. Coherent spin shuttling has been demonstrated at a transfer fidelity of 99.97% for spin eigenstates, and 98% for spin-superposition states [36, 37], while SWAP gates have also been shown to transport arbitrary qubit states with fidelity up to 84% [38]. In addition, silicon on insulator (SOI) nanowire and fin field-effect transistors (nwFET and finFET) devices [39–41] have been used to confine spin qubits within etched silicon structures, and have been proposed for sparsely-connected two-dimensional qubit architectures [42]. These devices typically show a large electrostatic gate control of the QDs (larger so-called lever arms α) which is advantageous for reflectometry readout techniques, or spin-photon coupling [43, 44].

To realise the qubit pipeline, we propose a sparse two-dimensional quantum dot (QD) array, which we refer to as a nanogrid (see Fig. 2 (a)). The nanogrid is a weaved grid of silicon ‘channels’ in which QDs can be formed (e.g. etched silicon in the case of nwFET and finFET approaches, or through confining depletion gates in the case of planar MOS). Metal gates (green and orange shapes) for forming QDs are placed along and over the exposed Si to form locally one-dimensional QD arrays,

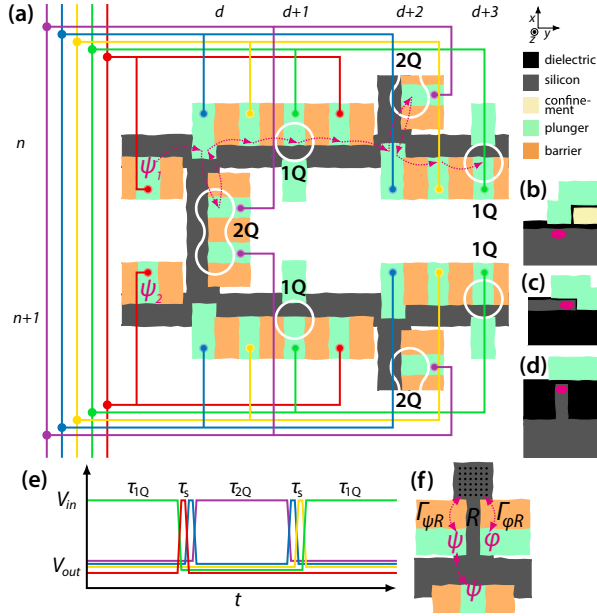


Figure 2. **Silicon quantum dot pipeline unit cell.** (a) Unit cell of a qubit pipeline, realised as a weaved grid of silicon channels (dark gray grid) which may be defined by etching or electrostatically by depletion gates (not shown). Overlapping metal gates (coloured rectangles) are used to confine, shuttle and manipulate electron spin qubits within the channels. Connectivity for five-stage shuttling is shown as colored lines where all sites mod 5 (for example, those controlling ψ_1 and ψ_6) are connected to the same voltage source. (b)-(d) Side views of different gate stacks which could be used in this implementation, including (b) planar MOS, (c) SOI nanowire, and (d) finFET. Quantum dots (magenta blobs) are confined using etched silicon or confinement gates (light yellow). (e) Sketch of the shuttling pulse sequence (relative pulse durations not to scale). Voltages V_{in} (V_{out}) are those at which single (zero) electron occupancy of the QD becomes the ground state. Single- and two-qubit gates are separated by short shuttling steps – in general, the number of shuttling steps depends on the exact gate layout, and depend on e.g. footprints required for routing. (f) Structures for local electron reservoirs (R), for spin readout (with an auxiliary state φ), and hence for preconfiguration of quantum states ψ . The operation of these structures, which can be placed along pipes between $d+1$ and $d+2$ (see panel (a)), is discussed further in the text.

which make 90-degree angles at T-junctions to join neighbouring pipes. Such weaving is required for entangling all the qubits from different pipes. Extra control from a second gate layer aids tuning all QDs to nominally identical setpoints despite variability in e.g. charging energies [45, 46]. The metal gates are routed with vias. The overall architecture can be realised in a variety of silicon QD platforms, including planar MOS, SOI, and finFETs, with cross-sections illustrated in Figures 2 (b)-(d). In addition, a similar layout can be used in a Si/SiGe architecture or indeed other types of electron or hole semiconductor spin qubits.

A. Shuttling

In the qubit pipeline, we shuttle electrons between different columns d where logical 1Q and 2Q gate operations are performed. Electrons can be shuttled from one QD to another by inverting the biasing between gates, i.e. by pulsing over the inter-dot charge transition with DQD charge occupancies $(1, 0) \rightarrow (0, 1)$ [47–49]. This scheme is also referred to as bucket-brigade shuttling.

The shuttling time τ_s is determined by the inter-site tunnel coupling frequency t_{ij}/h (typically 1 – 20 GHz in two-layer QD arrays using barrier gates [48]) and the electron temperature, which affects charge relaxation rates. Charge shuttling errors are expected to be minimized when the pulsing rate is slow compared to the inter-dot tunnel coupling [36, 50], where non-adiabatic Landau-Zener (LZ) transitions are minimal. At tunnel coupling $t_{ij}/h = 20$ GHz, the ramp can be performed adiabatically ($P_{LZ} < 10^{-4}$) with shuttling times of 9.1 ns or more (see Supplementary Sec. S2a). Electron charges and spins have been demonstrated to shuttle reliably over these timescales [36, 50], so we take 10 ns as the range of target shuttling times τ_s . The exact shuttling time should be determined to avoid LZ transitions to excited states, such as valley-orbit states. The systematic Z-phases arising from g -factor differences between sites can be accounted for as part of single-qubit control, as discussed in Sec. III C.

The pulse sequence depicted in Fig. 2 (e) can realise the shuttling and logic gate dynamics modulation. To this end, each gate is routed to an ac + dc voltage combining circuit. The ac nodes from gates from a single column, and mod 5 steps, are combined at interconnect level with a power splitter, whereas each gate receives an individual dc bias. Bias tees at gate nodes enable applying dc biases from individual dc sources. See Supplementary Sec. S2b for footprint estimates. As there are signals with three different periods, we could employ e.g. phase modulation or partially digital signal processing to generate the five shuttling biases, and hence shuttling biases for the entire pipeline with only three voltage pulse generators. We can fill the pipeline up to every fifth physical gate column of QDs single electrons, which we refer to as maximal filling.

B. Initialization, readout and pre-configuration

Initialisation and readout is analogous to a shift register for single-electron spins, where electrons are moved through a pipe and electron reservoirs are located at the input and output ends of the array. Preconfiguration of the unit cells can be done locally, utilizing initialization and readout nodes like the one depicted in Fig. 2 (f). Logical ground states $|\downarrow_q\rangle$ are initialised using spin-dependent reservoir-to-dot tunneling [51]. The fidelity is typically determined by the relative magnitude of the spin Zeeman energy splitting and $k_B T$ where T is the temperature of the electron reservoirs and k_B is Boltz-

mann's constant. For example, at $B_0 = 1$ T, $\mathcal{F} \geq 0.9999$ at $T \lesssim 73$ mK. The initialization time is determined by the reservoir-to-dot tunnelling time $1/\Gamma_{\psi_R}$, which can be controlled with a barrier gate, and can reach tens of GHz [52]. At higher electron reservoir temperatures, required fidelities could be obtained using real-time monitoring of the qubit through a negative-result measurement at the expense of longer initialization times [53].

For readout, we employ the so-called Elzerman readout, where we detect spin states using the reverse of the spin-dependent tunneling described above, detected by a capacitively-coupled charge sensor, such as a single-electron box [54, 55], at site φ (see Fig. 2 (f)). This method is estimated to yield a spin readout fidelity $\mathcal{F} \geq 0.993$ in ≤ 4 μ s [52], while advances in resonant readout techniques could help increase $\mathcal{F} \geq 0.9999$ in 50 ns [56]. We utilize Elzerman readout over Pauli spin blockade or parity readout, which are based on projections in the singlet-triplet basis, since we prefer to operate at relatively high B_0 fields, $B_0 \approx 1$ T.

C. Z-rotation gates with Stark-shifted g -factors

The electron spin g -factor g^* , which defines the Larmor frequency $\omega_0 = g^* \mu_B B_0 / \hbar$ (where μ_B is the Bohr magneton and B_0 the applied dc magnetic field) can be shifted using electric fields from gate voltages. In SiMOS heterostructures the dominant Stark shift is understood to arise from wavefunction displacement with respect to the Si/SiO₂ interface [57]. Linear or quasi-linear shifts $\delta g_q(V)$ with $\partial g / \partial E_z(V) = \pm(1-5) \times 10^{-3} \text{ (MV/m)}^{-1}$ have been reported for QDs in planar MOS devices [29, 58, 59] with an in-plane magnetic field and E_z applied perpendicular to the interface. The sign of the shift depends on the valley state of the electron [57, 58]. The roughness of the Si/SiO₂ interface also introduces some random contribution G_q to the effective g -factor, which can be larger than the tuneability, $G_q = \pm \mathcal{O}(10^{-3} \dots 10^{-2})$ [59]. Hence, the g -factor of a spin at some site q can be considered as a combination of these shifts on some intrinsic value, g_{Si} , such that $g_q^* = g_{\text{Si}} + G_q + \delta g_q(V)$. In the following, we assume $g_{\text{Si}} = 2.0$.

We use the gate-voltage controllable g -factor Stark shift to perform relative single-qubit $Z(\varphi_q) = e^{-i\varphi_q \sigma_z / 2}$ gates by synchronously shuttling the qubit onto a QD structure (see columns $d+1$ and $d+3$ in Fig. 2 (a)) with predetermined dc gate voltages. Spins encoding the qubit state remain at the same site for a fixed time τ_{1Q} to acquire some phase (relative to a spin with $g = g_{\text{Si}}$) before synchronously shuttling forward. The gate $Z(\varphi_q)$ is achieved by selecting a suitable g -factor shift

$$\delta g_q(V) = \frac{\varphi_q - 2\pi r_q}{\mu_B B_0 \tau_{1Q} \hbar^{-1}}. \quad (1)$$

Here, $r_q \in [0, 1)$ is selected from $G_q \mu_B B_0 \tau_{1Q} \hbar^{-1} := 2\pi(n_q + r_q)$, for $n_q \in \mathbb{Z}$. Since we only require phase matching up to 2π , the site-to-site randomness G_q only

contributes via $2\pi r_q$, which remains in the same order of magnitude for any G_q . As a result, the randomness does not affect the required tuneability to attain a rotation angle over a target gate time. Similarly, systematic phase shifts arising from the other QDs involved in shuttling can be accounted for as an effective contribution to G_q and corrected in the same way. The order of magnitude of $\delta g_q(V)$ required to generate a π phase shift at varying τ_{1Q} and B_0 is plotted in Fig. 3 (a), where we take $G_q = 0$ for simplicity. Tuneabilities of at least $\delta g \approx \pm 3.6 \times 10^{-5}$ and $\delta g \approx \pm 3.6 \times 10^{-4}$ are required at $B_0 = 1$ T for $\tau_{1Q} = 1$ μ s and $\tau_{1Q} = 0.1$ μ s, respectively.

To realise such Stark shifts, we propose to employ the plunger gate as the g -factor tuning gate, and a neighbouring gate as a μ -compensating gate (gate labelled with μ in Fig. 3 (b)). This additional compensating gate is required to ensure the electrochemical potentials (see Supplementary Sec. S3, Eqs. S1-S2), and hence QD electron occupancies remain correct under the applied electric field for g -factor tuning, as illustrated in the triple QD stability diagrams shown in Figs. 3 (c)-(d). In planar MOS, the plunger gate contributes dominantly to E_z , while the μ -compensating gate E-field mostly to E_x , at site q , having negligible effect on the g -factor. In etched silicon devices, due to two facets of Si/SiO₂ interface (Fig. 2 (f)), we expect both split gates to contribute to the Stark shift, but as long as the effects of the two gates to the g -factor Stark shift and the electrochemical potential shift are asymmetric, the pair of gates allows to compensate for the shift in the electrochemical potential.

Analytical estimates for the E -field derivatives $\partial E_z / \partial V_j$ and $\partial E_x / \partial V_j$ due to the plunger and μ -compensating voltages V_q and V_μ , as a function of longitudinal position x , close to the MOS interface, are plotted in Fig. 3 (e), with simulation details given in Supplementary Sec. S3. The estimated values of the E_z -gradient at site q , together with a conservative figure of $\partial g / \partial E_z = \pm 1 \times 10^{-3} \text{ (MV/m)}^{-1}$ suggest a required voltage shift $dV_q = 615 \text{ V} \times \delta g_q$. For example, a target Stark shift $\delta g_\pi = \pm 3.6 \times 10^{-5}$, would require the dc bias on the gate to be shifted $dV_q = \pm 22$ mV. The corresponding change in μ_q can be compensated with the μ -compensating gate, by setting the voltage $dV_\mu \approx -\alpha_{qq} / \alpha_{q\mu} dV_q$, where α_{ij} is the lever arm between QD at site i and gate j (see Supplementary Sec. S3).

We evaluate the sensitivity of this $Z(\varphi_q)$ gate to noise using the so-called process fidelity [60] between an ideal and a noisy unitary gate, for the case of $\tau_{1Q} = 1.0$ μ s and $B_0 = 1.0$ T. We sample a value for G_q from a normal distribution with width σ_G set to $10^{-3} g_{\text{Si}}$, and use it to find δg_q (Eq. (1)) to hit $\varphi_q = \pi$ for an ideal gate. For the noisy gate, we consider shuttling time errors of magnitude $\delta\tau$ that lead to gate time errors, and fluctuations in the gate voltage, δV_q , which lead to impacts in the g -factor according to $\delta g_q = \delta V_q / 615 \text{ V}$. These noise contributions $\delta\tau$ and δV_q are also sampled from normal distributions with varying widths of σ_τ and σ_V , respectively.

In Fig. 3 (f), we plot the resulting $Z(\pi)$ fidelities,

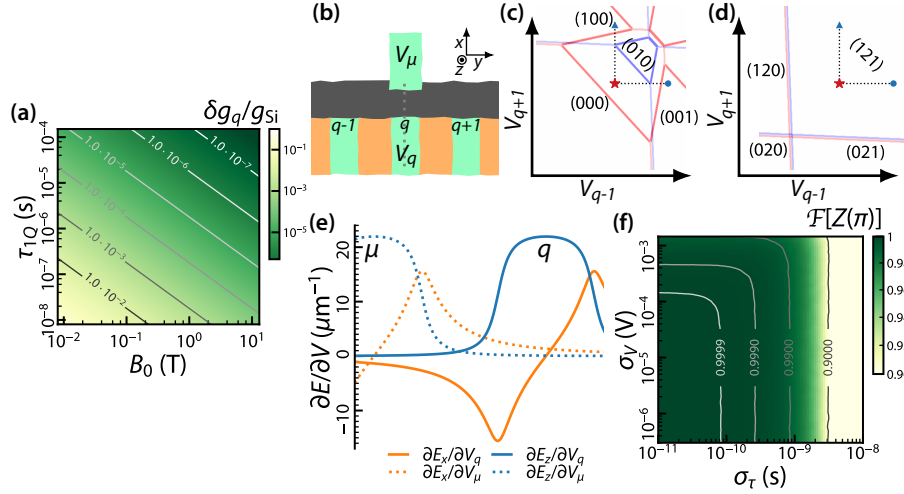


Figure 3. **Z-rotation gate using Stark shifts.** (a) Order of magnitude of Stark shift δg_q , with respect to the bulk value $g_{\text{Si}} \approx 2.0$, as a function of external magnetic field B_0 and single-qubit gate time τ_{1Q} , required for the π -rotation gate $Z(\pi)$. (b) Gate layout realisation of the g -factor tuning scheme with shuttling through quantum dots under gates $q-1$, to q , and to $q+1$. The voltage V_q is used to tune the g -factor at site q , while the voltage V_μ is used to compensate for the change in the electrochemical potential due to the g -factor tuning. (c)-(d) Overlaid stability diagrams of the $(q-1, q, q+1)$ triple quantum dot at the start and end (blue lines), and at the middle (red lines) of the shuttling sequence, illustrate the requirement for electrochemical potential compensation. Using a waveform as shown in Fig. 2 (e), shuttling proceeds from the charge configuration $(n_{q+1} n_q n_{q-1}) = (001)$ (blue circle marker) to (010) (red star marker), and to (100) (blue triangle marker). (c) In the perfectly compensated case with g -factor tuning, the (010) region opens up during the shuttling sequence. (d) In the non-compensated case, adjusting V_q to tune the g -factor at q causes the (010) region to shift away from the ground state charge configurations. (e) Electric field gradients evaluated along the cut shown as a gray dotted line in panel (d). Electric field gradients due to V_q are denoted as blue, and those due to V_μ as orange traces. (f) Estimated fidelity of $Z(\pi)$ as a function of variance in actual gate duration and voltage noise affecting δg , with fixed $\sigma_G = 10^{-3} g_{\text{Si}}$, $B_0 = 1$ T, and $\tau_{1Q} = 1$ μs . (see main text).

averaged over 1000 samples at each pair of noise levels. We find that the noise sources for the gate time and g -tuning errors add up independently. Noise levels of $\sigma_\tau \lesssim 0.08$ ns, i.e. $\sim 10^{-2} \tau_s$ for the target shuttling time of $\tau_s = 10$ ns, and $\sigma_V \lesssim 100$ μV are required to achieve $\mathcal{F}[Z(\varphi_q)] \geq 0.9999$. Charge noise acts equivalently to gate voltage fluctuations. Based on state-of-the-art charge noise spectral densities in industrial SiMOS devices [41, 61, 62], we would expect voltage fluctuations of $\sigma_V \approx 30\text{--}90$ μV over a bandwidth of 1 Hz – 1 GHz, which is sufficient for our fidelity requirements, whereas there is less experimental data available on timing errors in shuttling.

D. Two-qubit gate family with gate-voltage-tuneable exchange strength

To perform two-qubit operations, qubits are shuttled to neighbouring sites that connect adjacent pipes, in order to introduce an exchange interaction whose strength, J_{ij} , can be estimated by

$$J_{ij} \approx \frac{2t_{ij}^2 \Delta K}{[(\Delta K)^2 - \epsilon(t)^2]}. \quad (2)$$

Here, $\epsilon(t)$ is the detuning of the single-particle level spacings proportional to chemical potentials and ΔK is the difference between the on-site and inter-site charging energies. J_{ij} can thus be in-situ modulated by the detuning using the plunger gates, or the tunnel coupling using the barrier gates. Both knobs can modulate the exchange strength over several order of magnitude. We choose to use module the tunnel coupling to allow us to operate in the centre of the $(1, 1)$ charge configuration, where charge noise is minimised [63, 64].

In the logic basis $\{|\uparrow_i \uparrow_j\rangle, |\uparrow_i \downarrow_j\rangle, |\downarrow_i \uparrow_j\rangle, |\downarrow_i \downarrow_j\rangle\}$, the interaction between two exchange-coupled spins with a Zeeman energy difference ΔE_Z (see Supplementary Sec. S4a, Eq. (S8)) generates time-evolution which is analogous to the single-qubit semiclassical Rabi dynamics in the $m_z = 0$ subspace, while the decoupled $m_z = \pm 1$ subspaces merely acquire phases according to their Larmor frequencies (see Supplementary Sec. S4b, Eq. (S14)). In this analogy, within the $m_z = 0$ subspace, $\Delta_{ij} := \Delta E_Z + (J_i - J_j)/2 \approx \Delta E_Z$ (also see Supplementary Sec. S4a) corresponds to the qubit-drive detuning, J_{ij} to the transversal coupling strength, and $\Omega_{ij} = \sqrt{\Delta_{ij}^2 + J_{ij}^2}/\hbar$ to the Rabi frequency.

This time evolution is our native two-qubit operation. Figure 4 (a)-(d) illustrates some circuit identities obtained from it. To classify these operations, we may rep-

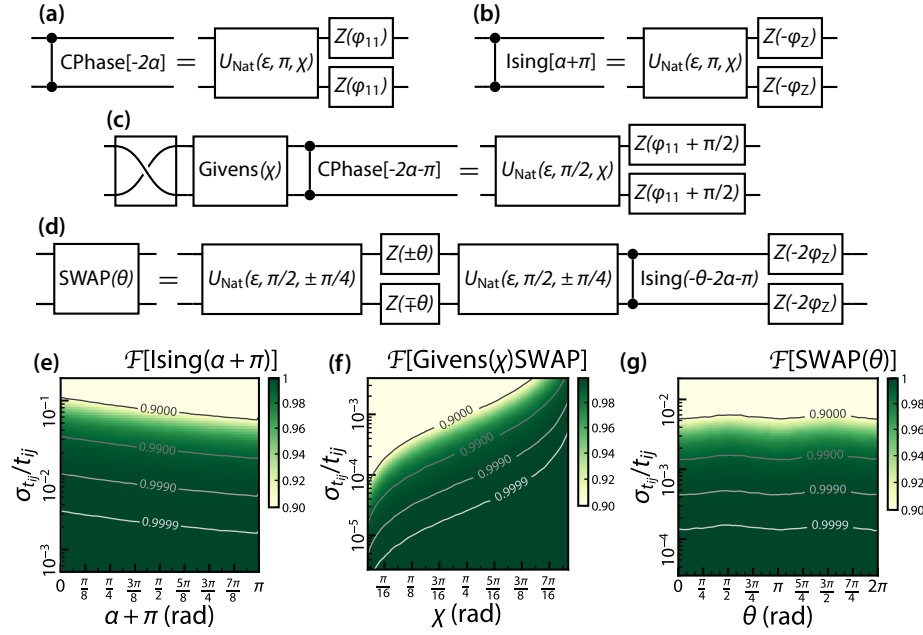


Figure 4. **Two-qubit gate family from nearest-neighbour exchange.** (a)-(d) Circuit identities for the unitary time evolution $U_{\text{NNE}}(\epsilon, \varphi, \chi)$ Eq. (3), describing nearest-neighbour exchange in the presence of Zeeman energy differences. Multiples of $2\pi n$ are left out of the rotation angles for simplicity. (a)-(b) Choice of rotation angle $\varphi = \pi + 2\pi n$ realises the phase gates (a) CPhase and (b) Ising ZZ -rotation gate. (c) Choice of $\varphi = \pi/2 + 2\pi n$ realises a gate close to the Givens rotation, where the rotation angle χ depends on the ratio $\Delta E_Z/J_{ij}$. (d) The SWAP-rotation gate can be constructed from the native unitary gate with $\varphi = \pi/2 + 2\pi n$ and $\chi = \pi/4$, as two such native operations separated by single-qubit Z -rotations. The phases of the $m_z = \pm 1$ components are fixed by subsequent application of another phase gate and single-qubit Z -rotations. (e)-(g) Fidelities for the native gates with (e) $\phi = \pi + 2\pi n$, realising the Ising ZZ -rotation gate, and (f) $\phi = \pi/2 + 2\pi n$, realising the Givens(χ) SWAP operation, which, for $\chi = \pi/4$ is used in the composition of SWAP(θ) (see panel (d)), and (g) the composite SWAP(θ) rotation gate as a function of rotation angles and tunnel coupling variance $\sigma_{t_{ij}}/t_{ij}$.

represent the unitary operation with two angle variables, as

$$U_{\text{Nat}}(\epsilon, \varphi, \chi) \hat{=} e^{i\varphi \cos(\chi)} \times \begin{pmatrix} e^{-i\varphi_Z - i\alpha(\varphi, \chi)} & 0 & 0 & 0 \\ 0 & [\cos(\varphi) + i\sin(\chi)\sin(\varphi)] & -i\cos(\chi)\sin(\varphi) & 0 \\ 0 & -i\cos(\chi)\sin(\varphi) & [\cos(\varphi) - i\sin(\chi)\sin(\varphi)] & 0 \\ 0 & 0 & 0 & e^{i\varphi_Z - i\alpha(\varphi, \chi)} \end{pmatrix}. \quad (3)$$

Here, the angle $\varphi = \tau_{2Q}/\Omega_{ij}$ is set by the gate time τ_{2Q} and the frequency Ω_{ij} . The angle $\chi = \arctan(x)$ is set by the ratio $x = \Delta_{ij}/J_{ij}$. This ratio is related to the single-qubit analogue of the B_1 polar angle $\arccos(\Delta_{ij}/\Omega_{ij})$ via $\arccos(\Delta_{ij}/\Omega_{ij}) = \text{arccot}(x)$. We also have $\varphi_Z = (E_Z + \Delta E_Z)/\Omega_{ij}$, and $\alpha(\varphi, \chi) = \varphi \cos(\chi)$. When $x \rightarrow 0$, coinciding with negligible Zeeman energy differences, the native operation (3) reduces to the SWAP-rotation with the rotation angle given by φ (viewed from the frame from which $E_Z = 0$). But even in the presence of ΔE_Z , the native operation (3) can be used to realise several familiar two-qubit operations.

One way to engineer desired gates starts by considering interaction times that correspond to particular numbers of completed rotations with respect to the single-qubit analogue of the Rabi frequency. In doing so, are left to fix

χ to define the operation. Since we largely do not control the Zeeman energy difference, we choose the polar angle analogue with J_{ij} . By choosing $\varphi = \pi + 2\pi n$, we realise the diagonal two-qubit phase gates [65], as

$$Z(\varphi_{11}) \otimes Z(\varphi_{11}) e^{-i\alpha - i\varphi} U_{\text{Nat}}(\epsilon = 0, \varphi = \pi + 2\pi n, \chi) = \text{CPhase}[-2\alpha(\varphi = \pi + 2\pi n, \chi)]. \quad (4)$$

where we have defined $\varphi_{11} = -\varphi_Z - \alpha(\varphi, \chi)$, and

$$Z(-\varphi_Z) \otimes Z(-\varphi_Z) U_{\text{Nat}}(\epsilon, \varphi = \pi + 2\pi n, \chi) = \text{Ising}[\alpha(\varphi = \pi + 2\pi n, \chi) + \pi]. \quad (5)$$

The circuits are visualised in Fig. 4 (a)-(b). See Supplementary Sec. S5 for their matrix representations. These gates are maximally entangling (for certain rotation angles), but e.g. the SWAP gate, or any non-diagonal gate using just phase gates and single-qubit Z -rotations is not possible. In general, a larger set of gates allows more efficient decompositions for algorithms. For example, the variational eigensolvers for the Fermi-Hubbard model natively decompose into SWAP-rotations and single-qubit Z -rotations, so we show how to construct the SWAP-rotation from the native operation.

By instead choosing $\varphi = \pi/2 + 2\pi n$, we obtain a gate close to the so-called Givens rotation (see Supplementary

Sec. S5, Eq. (S24)), as

$$\begin{aligned} & Z(\varphi_{11} + \pi/2) \otimes Z(\varphi_{11} + \pi/2) e^{-i\alpha + i\varphi} \times \\ & U_{\text{Nat}}(\epsilon, \varphi = \pi/2 + 2\pi n, \chi) = \\ & \text{CPhase}[-2\alpha(\pi/2 + 2\pi n, \chi) + \pi] \text{Givens}(\chi) \text{SWAP}. \end{aligned} \quad (6)$$

The circuit identity is illustrated in Fig. 4 (c). The angle of the Givens rotation is controllable with the polar angle analogue, although not all rotation angles are attainable equally easily. In particular, rotation angles of 0 and $\pi/2$ would require negligible Zeeman energy difference or exchange strength, respectively. However, these cases are not interesting, since in the absence of Zeeman energy differences, we may employ a SWAP-rotation gate, and in the absence of an interaction the operation is non-entangling.

The rotation angle $\chi = \pm\pi/4$ corresponds to the case where the (absolute value of the) Zeeman energy difference is equal to the exchange strength. Here, the $m_z = 0$ matrix elements simplify to $|U_{\text{Nat}}(\epsilon, \pi/2, \pi/4)_{ij}| = 1/\sqrt{2}$. The native operation $U_{\text{Nat}}(\epsilon, \pi/2, \pi/4)$ thus acts as a controlled Hadamard operation for the $m_z = 0$ subspace. The operation can be used to convert single-qubit $Z(\theta)$ -rotations into SWAP-rotations, as

$$\begin{aligned} \text{SWAP}(\theta) = & -e^{-i\theta \pm i\pi} Z(-2\varphi_Z) \otimes Z(-2\varphi_Z) \text{Ising}[-\theta - 2\alpha - 2\varphi] \times \\ & U_{\text{Nat}}\left(\epsilon, \frac{\pi}{2}, \pm\frac{\pi}{4}\right) Z(\pm\theta) \otimes Z(\mp\theta) U_{\text{Nat}}\left(\epsilon, \frac{\pi}{2}, \pm\frac{\pi}{4}\right). \end{aligned} \quad (7)$$

The circuit is illustrated in Fig. 4 (d). We have written the circuit identity using the Ising gate for clarity, but in realising it using Eq. (5), we may absorb the Z -rotations into the final step, reducing physical gates from 6 to 5. It provides an exact method to perform SWAP-rotation operations, including the non-entangling SWAP gate, in the presence of Zeeman energy differences. The fidelity of this operation does not depend on the magnitude of ΔE_Z (as long as an equally large exchange strength is attainable), which means that the gate decomposition can be used with e.g. micromagnets, with which $\Delta E_Z = \mathcal{O}(1 - 10 \text{ GHz})$ [38].

The strategy for choosing parameters for the $\varphi = \pi/2 + 2\pi n$ operation is as follows (also see Supplementary Sec. S6 for further details). Knowing ΔE_Z , we set $J_{ij} = |\Delta E_Z|$. We are required to set the gate time, as $\tau = (\pi/2 + 2\pi n)/(\sqrt{2}J_{ij})$. The gate time is limited by a minimum set by ΔE_Z , and a resolution $2\pi n/(\sqrt{2}J_{ij})$, but we may use g -factor tuneability at QD j for fine-tuning τ (after which J_{ij} is recalculated). Smaller g -factor tuneability then requires a longer gate time to minimise gate time errors.

For example, setting the target gate time and rotation angle, as $\tau = 1 \mu\text{s}$, and $\chi = \pi/4$, respectively, and assuming $\Delta K = 1 \text{ meV}$, $\sigma_G = 10^{-3}g_{\text{Si}}$, $B_0 = 1 \text{ T}$ yields the desired Givens-like gate with $x = \pm 1$, and with average exchange strength, number of rotations, and average

timing errors of $J_{ij} \approx 32 \text{ MHz}$, $n \approx 45$, and $\delta\tau_{2Q} \approx 0.1 \text{ ns}$. For the phase gates, the protocol is similar, but x is solved from the desired rotation angle. We note that typically, the two-qubit gates impose an independent restriction to the g -factor tuneability to ensure that fidelities are not limited by gate timing errors, which we find to be higher than the requirements for single-qubit gates. For example, in the above, we require approximately $\delta g \geq \pm 1 \times 10^{-4}$ (corresponding to $dV_q \leq \pm 61 \text{ mV}$).

The process fidelities of the native $\text{Ising}(\alpha + \pi)$, $\text{Givens}(\chi)\text{SWAP}$, and composite $\text{SWAP}(\theta)$ operations are shown in Fig. 4 (e)-(g), as a function of rotation angle and relative variance in tunnel coupling noise, $\sigma_{t_{ij}}/t_{ij}$. They are evaluated using the exact perturbative Hamiltonian (Supplementary Sec. S4, Eq. (S8)), at $\epsilon = 0$. We average over $N = 1000$ random g -factor pairs. For the Givens-like gate, we determine the sign of χ from the sign of the g -factor difference. All gates enable fidelities $\mathcal{F} \geq 0.9999$ for sufficiently low noise in the tunnel coupling. For example, charge noise in the barrier gate voltage propagates to noise in the tunnel coupling. The dependence of both rotation angles on tunnel coupling is reflected in the fidelities: angles that require higher t_{ij} are more sensitive to tunnel coupling noise. However, since the rotation angles of the SWAP-rotation gate (7) arise from single-qubit Z -rotations, it's fidelity is approximately independent of rotation angles, and expected to be limited by the fidelity of the $\text{Givens}(\chi)\text{SWAP}$ operation.

E. Transversal rotation gates

A gate set enabling universal quantum computing requires another single-qubit gate besides the $Z(\varphi_q)$ gate and a maximally entangling two-qubit gate [66]. To this end, we propose to realise a globally applied $\sqrt{X} = \mathbf{I}(1 + i)/2 + \sigma_x(1 - i)/2$. The gate composes into a single-qubit rotation gate e.g. via the identity $Y(\varphi_q) := \sqrt{X}Z(\varphi_q)\sqrt{X}^\dagger$.

In the nanogrid, a \sqrt{X} gate can be applied globally by providing a small B_1 perpendicular to B_0 from large resonant structures, such as a dielectric 3D cavity resonator [67], or a superconducting resonator based on a coplanar waveguide patterned e.g. over the metal gate layers [68], with a resonance frequency coinciding with the average qubit frequency $f_{\text{Si}} \approx 28 \text{ GHz}$, and a quality factor $Q \approx 100$ to cover a bandwidth of 280 MHz corresponding to $G_q \leq \pm 10^{-2}$ ($> 5\sigma_G$, assuming $\sigma_G = 10^{-3}g_{\text{Si}}$). Global control allows avoiding issues related to crosstalk and impedance matching, which would be a challenge with partially or fully local broadband structures [69].

The global X -control together with pipelining provides an extra limitation for the circuit compilation and density of pipelining. Since all qubits on the pipeline undergo

the \sqrt{X} pulses, the algorithms must be compiled with periodic X -control. A simple example code block for the pipelined, global- X -controlled compilation is given by

$$[Z(\theta_1), X(\pi/2), Z(\theta_2), Z(\theta_3), X(\pi/2), \text{Native}(\theta_4)] \times D/6, \quad (8)$$

where $\text{Native}(\theta_4)$ is a native two-qubit gate of the system, as discussed in Sec. III D. This code block allows pipelining at a filling density of one in every three (logical) columns. The code block (8) maps to an equal density of single-qubit Z -rotation gates, Y -rotation gates, and native two-qubit interactions. Due to the variations in g -factor discussed above, driving all spins with a single drive tone is challenging. We instead opt for multitone driving and frequency binning [70], which is discussed in Supplementary Sec. S8. We show that reaching $\mathcal{F} \geq 0.9999$ requires $\sigma_{B_1} < 0.1 \mu\text{T}$ and $\sigma_\tau < 0.2 \text{ ns}$.

IV. APPLICATION AS BESPOKE HARDWARE FOR A NISQ EIGENSOLVER

We summarise the proposed qubit control protocols for operating the silicon spin qubit pipeline from Sec. III in Table II. The requirements of synchronous shuttling, lack of local runtime control, and qubit frequency variability leads to protocols where we fix gate times and adjust qubit frequencies with dc voltage tuneable parameters, namely the g -factor (qubit frequency) and the exchange strength. Each of these protocols are feasible up to fidelities $\mathcal{F} \geq 0.9999$ in the presence of noise, in the realistic scenario where qubit frequency variabilities are larger than the frequency tuneability.

We now exemplify how these elements propagate into solving a quantum computing problem in the NISQ era. Here, we focus on the variational eigensolver for the Fermi-Hubbard model, where the resources required to run the algorithm on a set of physical qubits have been estimated in [18], and where the task is to estimate the ground state of a 5×5 Fermi-Hubbard Hamiltonian. See supplementary Sec. S9 for details of this algorithm. At the low level, the algorithm breaks down into SWAP-, and single-qubit Z -rotation gates for the so-called (simulated) state initialisation and (simulated) state evolution stages, while the bit-string (physical qubit) initialisation and readout stages also require qubit-selective qubit-flip $X(\pi)$ and basis-change $X(\pi/2)$ operations. We assume that we are not limited by initialisation or readout times. The single-qubit gate times, and the two-qubit gate time errors are upper limited by the qubit frequency tuneability. While the tuneability has not been studied on a large number of devices, based on the literature, we expect the processor clocks speeds no slower than 1 MHz (at $B_0 = 1 \text{ T}$). This means that to run an algorithm of depth 10000, for example, we require qubit $T_2^* \geq 10 \text{ ms}$.

We summarise the estimated pipelined run-time, and contributions to the run-time, of the Fermi-Hubbard variational eigensolver in Table III, using the resource esti-

mates from [18]. There are several layers at the high level. The algorithm requires a number of *iterations*. Each iteration consists of a number of *runs*, which is equal to the number of circuit configurations multiplied by runs per configuration. The number of *circuit configurations*, in turn, is determined by the number of parameters, number of measured observables, and the number of noise levels, which is part of an error mitigation protocol [71]. The number of *runs per configuration* is determined by the number of runs for one parameter, to measure one set of commuting observables, and the extra sampling cost for error mitigation. For each parameter-observable-set-specific run, we may then evaluate the circuit run time.

Two types of classical parallelisation are possible. As discussed in Sec. II, pipelining allows to perform N_r number of repetitions for a circuit of depth D in time $(D + N_r)\tau$. For example, at maximal filling, this run-time scaling is $(D + 2N_r)\tau$. For single-qubit and two-qubit gate depths of D_{1Q} and D_{2Q} , the run-time for N_r repetitions on the nanogrid pipeline (Fig. 2 (a)) with three physical shuttling steps between gates is then $(D_{1Q} + 2N_r)(\tau_{1Q} + 3\tau_s) + (D_{2Q} + 2N_r)(\tau_{2S} + 3\tau_s)$. For $D_{1Q} = 1174$ and $D_{2Q} = 2196$ [18], and the gate time estimates for Z -rotation and SWAP-rotation gates from Table II, we find that pipelining reduces the run-time per circuit configuration from 25.5 minutes (assuming $\tau_{1Q} = 1 \mu\text{s}$) to 1.74 seconds, i.e. by roughly a factor of 880.

We may also run e.g. different circuit configurations on different physical pipeline processors in parallel. To estimate the footprint of the pipeline processor, we expect the width of a single pipe to be approximately 340 nm, with a same-layer gate pitch of 100 nm. Likewise, we expect the length of a single-qubit or two-qubit gate step to be approximately 190 nm. Then, for $N = 25$ qubits, and a circuit depth of $D = D_1 + D_2 = 1174 + 2196 = 3370$ quantum logic gates, we estimate the footprint of a single pipeline qubit processor to be $8.5 \mu\text{m} \times 640.3 \mu\text{m}$.

V. CONCLUSIONS AND DISCUSSION

We have analysed a qubit pipeline architecture for realizing gate based quantum computation in the NISQ era. The architecture minimizes run-time local control resources, utilizing instead global run-time, and local pre-configuration control. This is made possible by a combination of an increased qubit grid layout size, and by synchronized operation, where steps of qubit state shuttling and quantum logic gates alternate.

Having described the architectural paradigm, we focused on a physical implementation case-study in the SiMOS electron spin qubit platform. Here, we laid out qubit control protocols under the pipeline- and platform-specific restrictions, demonstrating each theoretically with NISQ-high fidelities while remaining robust against qubit frequency variabilities characteristic for the platform. Our main focus has been to address this frequency

Operation	Symbol	Time	Method
Shuttling	τ_s	10 ns	Global bucket-brigade pulses
Single-qubit Z -rotations	τ_{1Q}	1 μ s (0.1 μ s)	Local g -factor Stark shifts
Single-qubit X -rotations	τ_{1X}	$3\tau_{1Q} + 8\tau_s = 3.06 \mu$ s (0.36 μ s)	Global B_1 -drive frequency bins
Two-qubit native gates	τ_{2Q}	1 μ s (0.1 μ s)	Native exchange interaction
Two-qubit phase gates	τ_{2P}	$\tau_{2Q} + \tau_{1Q} + 3\tau_s = 2.0 \mu$ s (0.23 μ s)	Composite from native gates and Z -rotations
Two-qubit SWAP-rotations	τ_{2S}	$3\tau_{2Q} + 2\tau_{1Q} + 12\tau_s = 5.1 \mu$ s (0.62 μ s)	Composite from native gates and Z -rotations

Table II. **Qubit control protocols on the pipeline.** Summary of the protocols introduced in Section III. We have marked the gate times assuming $\tau_{1Q} = \tau_{2Q} = 0.1 \mu$ s in parenthesis. Numbers that are not in parentheses assume $\tau_{1Q} = \tau_{2Q} = 1 \mu$ s. Faster gate times require higher attainable g -factor tuning to prevent gate time errors from dominating the infidelities.

Eigensolver flow level	Symbol	Run-time overhead	Pipelined run-time overhead
Run-time per circuit configuration	τ_{config}	$[D_{1Q}(\tau_{1Q} + 3\tau_s) + D_{2Q}(\tau_{2S} + 3\tau_s)]N_{\text{reps}}$ = 26 minutes (3.8 minutes)	$[(D_{1Q} + 2N_{\text{reps}})(\tau_{1Q} + 3\tau_s) + (D_{2Q} + 2N_{\text{reps}})(\tau_{2S} + 3\tau_s)]$ = 1.7 seconds (0.25 seconds)
Circuit configurations	N_{configs}	3900	3900
Iterations	N_{iters}	100	100
Total run-time	τ_{run}	$N_{\text{iters}}N_{\text{configs}}\tau_{\text{config}}$ = 230 months (35 months)	$N_{\text{iters}}N_{\text{configs}}\tau_{\text{config}}$ = 7.9 days (11 hours)

Table III. **NISQ Fermi-Hubbard eigensolver run-time on the pipeline.** The times in parentheses assume $\tau_{1Q} = \tau_{2Q} = 0.1 \mu$ s, whereas otherwise we assume, that $\tau_{1Q} = \tau_{2Q} = 1 \mu$ s.

variability, while we may improve robustness against noise with bespoke control methods in the future. Most of the elements are possible to implement with present-day technology without further advances, but we expect more microwave engineering efforts to designing and testing switchable, dense transmission lines or resonators, and their ability to support a finite frequency bin. We then assessed the performance of this architecture for a NISQ variational eigensolver task. In the future, it may be possible to decrease the number of required gates per run by more directly utilising the native two-qubit gate family that arises from nearest neighbour exchange in the presence of Zeeman energy differences. The silicon spin qubit platform is well-suited to the pipeline approach, but the concept may also be implemented in other architectures, such as with trapped ions, or with superconducting qubits by replacing shuttling with SWAPs.

Indeed it would be an interesting topic of further work to explore an implementation based on SWAPs. There, the qubit grid remains fully occupied and stationary, and useful quantum information is transferred forward through the array (while states carrying no quantum information propagate in reverse). As before, the horizontal density of quantum information in the array can be ad-

justed as required (e.g. to accommodate initialisation and measurement times) by introducing buffer states which do not participate in the calculation. Back-propagating states or buffer states do not interfere with the calculation due to the non-entangling nature of the SWAP gate.

VI. ACKNOWLEDGEMENTS

Balint Koczor is acknowledged for a useful discussion regarding gate fidelities. SMP acknowledges the Engineering and Physical Sciences Research Council (EPSRC) through the Centre for Doctoral Training in Delivering Quantum Technologies (EP/L015242/1). MFGZ acknowledges support from UKRI Future Leaders Fellowship [grant number MR/V023284/1].

-
- [1] Preskill, J. **Quantum computing and the entanglement frontier**. *arXiv:1203.5813* **2012**,
- [2] Lloyd, S. **Ultimate physical limits to computation**. *Nature* **2000**, *406*, 1047.
- [3] Mizel, A.; Lidar, D. A.; Mitchell, M. **Simple proof of equivalence between adiabatic quantum computation and the circuit model**. *Physical review letters* **2007**, *99*, 070502.
- [4] Nielsen, M. A. **Cluster-state quantum computation**. *Reports on Mathematical Physics* **2006**, *57*, 147–161.
- [5] Deutsch, D. E. **Quantum computational networks**. *Proceedings of the Royal Society of London. A. Mathematical and Physical Sciences* **1989**, *425*, 73–90.
- [6] Undseth, B.; Xue, X.; Mehmandoust, M.; Rimbach-Russ, M.; Eendebak, P. T.; Samkharadze, N.; Sammak, A.; Dobrovitski, V. V.; Scappucci, G.; Vandersypen, L. M. **Nonlinear Response and Crosstalk of Electrically Driven Silicon Spin Qubits**. *Physical Review Applied* **2023**, *19*, 044078.
- [7] Gonzalez-Zalba, M.; de Franceschi, S.; Charbon, E.; Meunier, T.; Vinet, M.; Dzurak, A. **Scaling silicon-based quantum computing using CMOS technology**. *Nature Electronics* **2021**, *4*, 872–884.
- [8] Benjamin, S. **Schemes for parallel quantum computation without local control of qubits**. *Physical Review A* **2000**, *61*, 020301.
- [9] Benjamin, S. C. **Quantum Computing Without Local Control of Qubit-Qubit Interactions**. *Physical review letters* **2001**, *88*, 017904.
- [10] Fitzsimons, J.; Twamley, J. **Globally Controlled Quantum Wires for Perfect Qubit Transport, Mirroring, and Computing**. *Physical review letters* **2006**, *97*, 090502.
- [11] Laucht, A.; Muhonen, J. T.; Mohiyaddin, F. A.; Kalra, R.; Dehollain, J. P.; Freer, S.; Hudson, F. E.; Veldhorst, M.; Rahman, R.; Klimeck, G., et al. **Electrically controlling single-spin qubits in a continuous microwave field**. *Science advances* **2015**, *1*, e1500022.
- [12] Wolfowicz, G.; Urdampilleta, M.; Thewalt, M. L. W.; Riemann, H.; Abrosimov, N. V.; Becker, P.; Pohl, H.-J.; Morton, J. J. L. **Conditional control of donor nuclear spins in silicon using stark shifts**. *Physical Review Letters* **2014**, *113*, 157601.
- [13] Hansen, I.; Seedhouse, A. E.; Saraiva, A.; Laucht, A.; Dzurak, A. S.; Yang, C. H. **Pulse engineering of a global field for robust and universal quantum computation**. *Physical Review A* **2021**, *104*, 062415.
- [14] Lim, Y. L.; Beige, A.; Kwek, L. C. **Repeat-until-success linear optics distributed quantum computing**. *Physical review letters* **2005**, *95*, 030505.
- [15] Moehring, D. L.; Maunz, P.; Olmschenk, S.; Younge, K. C.; Matsukevich, D. N.; Duan, L.-M.; Monroe, C. **Entanglement of single-atom quantum bits at a distance**. *Nature* **2007**, *449*, 68–71.
- [16] Campagne-Ibarcq, P.; Zalys-Geller, E.; Narla, A.; Shankar, S.; Reinhold, P.; Burkhardt, L.; Axline, C.; Pfaff, W.; Frunzio, L.; Schoelkopf, R. J.; Devoret, M. H. **Deterministic Remote Entanglement of Superconducting Circuits through Microwave Two-Photon Transitions**. *Phys. Rev. Lett.* **2018**, *120*, 200501.
- [17] Bernien, H.; Hensen, B.; Pfaff, W.; Koolstra, G.; Blok, M. S.; Robledo, L.; Taminiau, T. H.; Markham, M.; Twitchen, D. J.; Childress, L., et al. **Heralded entanglement between solid-state qubits separated by three metres**. *Nature* **2013**, *497*, 86–90.
- [18] Cai, Z. **Resource Estimation for Quantum Variational Simulations of the Hubbard Model**. *Physical Review Applied* **2020**, *14*, 014059.
- [19] Cade, C.; Mineh, L.; Montanaro, A.; Stanisic, S. **Strategies for solving the Fermi-Hubbard model on near-term quantum computers**. *arXiv preprint arXiv:1912.06007* **2019**,
- [20] Kivlichan, I. D.; McClean, J.; Wiebe, N.; Gidney, C.; Aspuru-Guzik, A.; Chan, G. K.-L.; Babbush, R. **Quantum simulation of electronic structure with linear depth and connectivity**. *Physical review letters* **2018**, *120*, 110501.
- [21] There is no guarantee that mapping the two-dimensional Fermi-Hubbard model to a connected two-dimensional qubit lattice offers an overall advantage over a one-dimensional qubit array [72]. This is intuitively related to the non-local nature of fermions, which has to be encoded in the simulation of fermionic charge degrees of freedom. Attempts to reconcile this intrinsic non-locality with the two-dimensional-lattice qubit layout would lead to encoding schemes that offer a better circuit depth scaling, but at a cost of almost doubling the numbers of qubits [72, 73], thus not necessarily reducing the overall circuit size. This complication is absent in the simpler one-dimensional qubit array, which instead requires additional Fermionic SWAP operations to represent the original connectivity.
- [22] Seidler, I.; Struck, T.; Xue, R.; Focke, N.; Trelenkamp, S.; Bluhm, H.; Schreiber, L. R. **Conveyor-mode single-electron shuttling in Si/SiGe for a scalable quantum computing architecture**. *npj Quantum Information* **2022**, *8*, 1–7.
- [23] McArdle, S.; Endo, S.; Aspuru-Guzik, A.; Benjamin, S. C.; Yuan, X. **Quantum computational chemistry**. *Reviews of Modern Physics* **2020**, *92*, 015003.
- [24] Harrow, A. W.; Hassidim, A.; Lloyd, S. **Quantum algorithm for linear systems of equations**. *Physical review letters* **2009**, *103*, 150502.
- [25] Li, R.; Petit, L.; Franke, D. P.; Dehollain, J. P.; Helsen, J.; Steudtner, M.; Thomas, N. K.; Yoscovits, Z. R.; Singh, K. J.; Wehner, S., et al. **A crossbar network for silicon quantum dot qubits**. *Science advances* **2018**, *4*, eaar3960.
- [26] Vandersypen, L.; Bluhm, H.; Clarke, J.; Dzurak, A.; Ishihara, R.; Morello, A.; Reilly, D.; Schreiber, L.; Veldhorst, M. **Interfacing spin qubits in quantum dots and donors—hot, dense, and coherent**. *npj Quantum Information* **2017**, *3*, 34.
- [27] Boter, J. M.; Dehollain, J. P.; Van Dijk, J. P.; Xu, Y.; Hensgens, T.; Versluis, R.; Naus, H. W.; Clarke, J. S.; Veldhorst, M.; Sebastiano, F., et al. **Spiderweb array: A sparse spin-qubit array**. *Physical Review Applied* **2022**, *18*, 024053.
- [28] Li, R.; Stuyck, N. D.; Kubicek, S.; Jussot, J.; Chan, B.; Mohiyaddin, F.; Elsayed, A.; Shehata, M.; Simion, G.; Godfrin, C., et al. **A flexible 300 mm integrated Si MOS platform for electron-and hole-spin qubits exploration**. 2020 IEEE International Electron Devices Meet-

- ing (IEDM). 2020; pp 38–3.
- [29] Veldhorst, M.; Hwang, J. C. C.; Yang, C. H.; Leenstra, A. W.; de Ronde, B.; Dehollain, J. P.; Muhonen, J. T.; Hudson, F. E.; Itoh, K. M.; Morello, A. t. **An addressable quantum dot qubit with fault-tolerant control-fidelity**. *Nature nanotechnology* **2014**, *9*, 981.
 - [30] Lawrie, W.; Eenink, H.; Hendrickx, N.; Boter, J.; Petit, L.; Amitonov, S.; Lodari, M.; Paquelet Wuetz, B.; Volk, C.; Philips, S., et al. **Quantum dot arrays in silicon and germanium**. *Applied Physics Letters* **2020**, *116*, 080501.
 - [31] Xue, X.; Russ, M.; Samkharadze, N.; Undseth, B.; Sammak, A.; Scappucci, G.; Vandersypen, L. M. K. **Quantum logic with spin qubits crossing the surface code threshold**. *Nature* **2022**, *601*, 343–347.
 - [32] Yang, C. H.; Chan, K. W.; Harper, R.; Huang, W.; Evans, T.; Hwang, J. C. C.; Hensen, B.; Laucht, A.; Tantt, T.; Hudson, F. E., et al. **Silicon qubit fidelities approaching incoherent noise limits via pulse engineering**. *Nature Electronics* **2019**, *2*, 151–158.
 - [33] Tantt, T. et al. Stability of high-fidelity two-qubit operations in silicon. *arXiv preprint arXiv:2303.04090* **2023**.
 - [34] Yoneda, J.; Takeda, K.; Otsuka, T.; Nakajima, T.; Delbecq, M. R.; Allison, G.; Honda, T.; Kadera, T.; Oda, S.; Hoshi, Y. t. **A quantum-dot spin qubit with coherence limited by charge noise and fidelity higher than 99.9%**. *Nature nanotechnology* **2018**, *13*, 102.
 - [35] Mills, A. R.; Guinn, C. R.; Gullans, M. J.; Sigillito, A. J.; Feldman, M. M.; Nielsen, E.; Petta, J. R. **Two-qubit silicon quantum processor with operation fidelity exceeding 99%**. *Science Advances* **2022**, *8*, eabn5130.
 - [36] Yoneda, J.; Huang, W.; Feng, M.; Yang, C. H.; Chan, K. W.; Tantt, T.; Gilbert, W.; Leon, R.; Hudson, F.; Itoh, K., et al. **Coherent spin qubit transport in silicon**. *Nature communications* **2021**, *12*, 4114.
 - [37] Noiri, A.; Takeda, K.; Nakajima, T.; Kobayashi, T.; Sammak, A.; Scappucci, G.; Tarucha, S. **A shuttling-based two-qubit logic gate for linking distant silicon quantum processors**. *arXiv preprint arXiv:2202.01357* **2022**.
 - [38] Sigillito, A. J.; Gullans, M. J.; Edge, L. F.; Borselli, M.; Petta, J. R. **Coherent transfer of quantum information in a silicon double quantum dot using resonant SWAP gates**. *npj Quantum Information* **2019**, *5*, 1–7.
 - [39] Corna, A.; Bourdet, L.; Maurand, R.; Crippa, A.; Kotekar-Patil, D.; Bohuslavskyi, H.; Laviéville, R.; Hutin, L.; Barraud, S.; Jehl, X., et al. **Electrically driven electron spin resonance mediated by spin–valley–orbit coupling in a silicon quantum dot**. *npj quantum information* **2018**, *4*, 1–7.
 - [40] Camenzind, L. C.; Geyer, S.; Fuhrer, A.; Warburton, R. J.; Zumbühl, D. M.; Kuhlmann, A. V. **A spin qubit in a fin field-effect transistor**. *arXiv:2103.07369* **2021**.
 - [41] Zwerver, A.; Krähenmann, T.; Watson, T.; Lampert, L.; George, H. C.; Pillarisetty, R.; Bojarski, S.; Amin, P.; Amitonov, S.; Boter, J., et al. **Qubits made by advanced semiconductor manufacturing**. *Nature Electronics* **2022**, *5*, 184–190.
 - [42] Crawford, O.; Cruise, J.; Mertig, N.; Gonzalez-Zalba, M. **Compilation and scaling strategies for a silicon quantum processor with sparse two-dimensional connectivity**. *arXiv preprint arXiv:2201.02877* **2022**.
 - [43] Vigneau, F.; Fedele, F.; Chatterjee, A.; Reilly, D.; Kuemmeth, F.; Gonzalez-Zalba, F.; Laird, E.; Ares, N. **Probing quantum devices with radio-frequency reflectometry**. *arXiv preprint arXiv:2202.10516* **2022**.
 - [44] Burkard, G.; Gullans, M. J.; Mi, X.; Petta, J. R. **Superconductor–semiconductor hybrid-circuit quantum electrodynamics**. *Nature Reviews Physics* **2020**, *2*, 129–140.
 - [45] Yang, T.-Y.; Ruffino, A.; Michniewicz, J.; Peng, Y.; Charbon, E.; Gonzalez-Zalba, M. F. **Quantum transport in 40-nm MOSFETs at deep-cryogenic temperatures**. *IEEE Electron Device Letters* **2020**, *41*, 981–984.
 - [46] Bavdaz, P. L.; Eenink, H. G. J.; van Staveren, J.; Lodari, M.; Almudever, C. G.; Clarke, J. S.; Sebastiano, F.; Veldhorst, M.; Scappucci, G. **A quantum dot crossbar with sublinear scaling of interconnects at cryogenic temperature**. *arXiv preprint arXiv:2202.04482* **2022**.
 - [47] Baart, T. A.; Shafiei, M.; Fujita, T.; Reichl, C.; Wegscheider, W.; Vandersypen, L. M. K. **Single-spin CCD**. *Nature nanotechnology* **2016**, *11*, 330.
 - [48] Baart, T. A.; Jovanovic, N.; Reichl, C.; Wegscheider, W.; Vandersypen, L. M. K. **Nanosecond-timescale spin transfer using individual electrons in a quadruple-quantum-dot device**. *Applied Physics Letters* **2016**, *109*, 043101.
 - [49] Zwerver, A. M. J.; Amitonov, S. V.; de Snoo, S. L.; Mądzik, M. T.; Russ, M.; Sammak, A.; Scappucci, G.; Vandersypen, L. M. K. **Shuttling an electron spin through a silicon quantum dot array**. 2022.
 - [50] Mills, A. R.; Zajac, D. M.; Gullans, M. J.; Schupp, F. J.; Hazard, T. M.; Petta, J. R. **Shuttling a single charge across a one-dimensional array of silicon quantum dots**. *Nature communications* **2019**, *10*, 1063.
 - [51] Elzerman, J. M.; Hanson, R.; Van Beveren, L. H.; Willems, Witkamp, B.; Vandersypen, L. M. K.; Kouwenhoven, L. P. **Single-shot read-out of an individual electron spin in a quantum dot**. *nature* **2004**, *430*, 431–435.
 - [52] Oakes, G.; Ciriano-Tejel, V.; Wise, D.; Fogarty, M.; Lundberg, T.; Lainé, C.; Schaal, S.; Martins, F.; Ibberson, D.; Hutin, L., et al. **Fast high-fidelity single-shot readout of spins in silicon using a single-electron box**. *Physical Review X* **2023**, *13*, 011023.
 - [53] Johnson, M. A.; Mądzik, M. T.; Hudson, F. E.; Itoh, K. M.; Jakob, A. M.; Jamieson, D. N.; Dzurak, A.; Morello, A. **Beating the thermal limit of qubit initialization with a Bayesian Maxwell’s demon**. *Physical Review X* **2022**, *12*, 041008.
 - [54] Borjans, F.; Mi, X.; Petta, J. **Spin digitizer for high-fidelity readout of a cavity-coupled silicon triple quantum dot**. *Physical Review Applied* **2021**, *15*, 044052.
 - [55] Ciriano-Tejel, V. N.; Fogarty, M. A.; Schaal, S.; Hutin, L.; Bertrand, B.; Ibberson, L.; Gonzalez-Zalba, M. F.; Li, J.; Niquet, Y.-M.; Vinet, M., et al. **Spin Readout of a CMOS Quantum Dot by Gate Reflectometry and Spin-Dependent Tunneling**. *PRX Quantum* **2021**, *2*, 010353.
 - [56] von Horstig, F.-E.; Ibberson, D. J.; Oakes, G. A.; Cochrane, L.; Stelmashenko, N.; Barraud, S.; Robinson, J. A.; Martins, F.; Gonzalez-Zalba, M. F. **Multi-module microwave assembly for fast read-out and charge noise characterization of silicon quantum dots**. *arXiv preprint arXiv:2304.13442* **2023**.
 - [57] Ruskov, R.; Veldhorst, M.; Dzurak, A. S.; Tahan, C. **Electron g-factor of valley states in realistic silicon quantum dots**. *Physical Review B* **2018**, *98*, 245424.
 - [58] Veldhorst, M.; Ruskov, R.; Yang, C. H.; Hwang, J. C. C.; Hudson, F. E.; Flatté, M. E.; Tahan, C.; Itoh, K. M.;

- Morello, A.; Dzurak, A. S. **Spin-orbit coupling and operation of multivalley spin qubits**. *Physical Review B* **2015**, *92*, 201401.
- [59] Ferdous, R.; Chan, K. W.; Veldhorst, M.; Hwang, J. C. C.; Yang, C. H.; Sahasrabudhe, H.; Klimeck, G.; Morello, A.; Dzurak, A. S.; Rahman, R. **Interface-induced spin-orbit interaction in silicon quantum dots and prospects for scalability**. *Physical Review B* **2018**, *97*, 241401.
- [60] Mayer, K.; Knill, E. **Quantum process fidelity bounds from sets of input states**. *Physical Review A* **2018**, *98*, 052326.
- [61] Elsayed, A.; Shehata, M.; Godfrin, C.; Kubicek, S.; Massar, S.; Canvel, Y.; Jussot, J.; Simion, G.; Mongillo, M.; Wan, D., et al. **Low charge noise quantum dots with industrial CMOS manufacturing**. *arXiv preprint arXiv:2212.06464* **2022**,
- [62] Spence, C.; Cardoso-Paz, B.; Michal, V.; Chanrion, E.; Niegemann, D. J.; Jadot, B.; Mortemousque, P.-A.; Klemm, B.; Thiney, V.; Bertrand, B., et al. **Probing charge noise in few electron CMOS quantum dots**. *arXiv preprint arXiv:2209.01853* **2022**,
- [63] Reed, M.; Maune, B.; Andrews, R.; Borselli, M.; Eng, K.; Jura, M.; Kiselev, A.; Ladd, T.; Merkel, S.; Milosavljevic, I., et al. **Reduced sensitivity to charge noise in semiconductor spin qubits via symmetric operation**. *Physical review letters* **2016**, *116*, 110402.
- [64] Martins, F.; Malinowski, F. K.; Nissen, P. D.; Barnes, E.; Fallahi, S.; Gardner, G. C.; Manfra, M. J.; Marcus, C. M.; Kuemmeth, F. **Noise suppression using symmetric exchange gates in spin qubits**. *Physical review letters* **2016**, *116*, 116801.
- [65] Meunier, T.; Calado, V. E.; Vandersypen, L. M. K. **Efficient controlled-phase gate for single-spin qubits in quantum dots**. *Physical Review B* **2011**, *83*, 121403.
- [66] Barenco, A.; Bennett, R., C. H. Cleve; DiVincenzo, D. P.; Margolus, P., N. Shor; Sleator, T.; Smolin, J. A.; Weinfurter, H. **Elementary gates for quantum computation**. *Physical Review A* **1995**, *52*, 3457–3467.
- [67] Vahapoglu, E.; Slack-Smith, J.; Leon, R. C.; Lim, W. H.; Hudson, F.; Day, T.; Cifuentes, J.; Tanttu, T.; Yang, C.-H.; Saraiva, A., et al. **Coherent control of electron spin qubits in silicon using a global field**. *npj Quantum Information* **2022**, *8*, 126.
- [68] Rausch, D. S.; Thiemann, M.; Dressel, M.; Bothner, D.; Koelle, D.; Kleiner, R.; Scheffler, M. **Superconducting coplanar microwave resonators with operating frequencies up to 50 GHz**. *Journal of Physics D: Applied Physics* **2018**, *51*, 465301.
- [69] Dehollain, J. P.; Pla, J. J.; Siew, E.; Tan, K. Y.; Dzurak, A. S.; Morello, A. **Nanoscale broadband transmission lines for spin qubit control**. *Nanotechnology* **2012**, *24*, 015202.
- [70] Fogarty, M. A. **Silicon edge-dot architecture for quantum computing with global control and integrated trimming**. *arXiv preprint arXiv:2208.09172* **2022**,
- [71] Cai, Z. **Multi-exponential error extrapolation and combining error mitigation techniques for nisq applications**. *npj Quantum Information* **2021**, *7*, 80.
- [72] Steudtner, M.; Wehner, S. **Quantum codes for quantum simulation of fermions on a square lattice of qubits**. *Physical Review A* **2019**, *99*, 022308.
- [73] Derby, C.; Klassen, J. **Low Weight Fermionic Encodings for Lattice Models**. *arXiv:2003.06939 [quant-ph]* **2020**,

Supplement for Pipeline quantum processor architecture for silicon spin qubits

S. M. Patomäki,^{1,2} M. F. Gonzalez-Zalba,¹ M. A. Fogarty,¹ Z. Cai,^{1,3} S. C. Benjamin,^{1,3} and John J. L. Morton^{1,2}

¹ Quantum Motion, 9 Sterling Way, London N7 9HJ, United Kingdom

² London Centre for Nanotechnology, University College London, London WC1H 0AH, United Kingdom*

³ Department of Materials, University of Oxford, Parks Road, Oxford OX1 3PH, United Kingdom

(Dated: June 14, 2023)

CONTENTS

S. Supplementary information	1
1. Programmable pixelgrid	1
2. Shuttling	1
a. Minimizing shuttling errors	1
b. Control line footprints	1
3. Electric field dependence on applied gate voltages	2
4. Nearest-neighbour exchange	3
a. Nearest-neighbour Hamiltonian	3
b. Native two-qubit unitary operation	3
5. Two-qubit gates	4
6. Engineering the native operation	4
7. Semiclassical Rabi model	4
8. Multitone driving with frequency binning	5
9. Variational quantum eigensolvers	7
References	7

Appendix S: Supplementary information

1. Programmable pixelgrid

We obtain an algorithm decomposition-reconfigurable pipeline using a dense 2D array of quantum dot defining metal gates. We outline this so-called pixelgrid in Fig. S1. Gate voltages determine which sites act as pipes, and which stages of the algorithm contain two-qubit gates. The design has the advantage of optimising gate decompositions, but the disadvantages associated with maximal density, such as crosstalk, and highly specialised demands for the fabrication of routing. Such routing demands have thus far only been demonstrated for $2 \times N$ QD arrays [1, 2].

2. Shuttling

a. Minimizing shuttling errors

As discussed in the main text, non-adiabatic time evolution can create shuttling errors via so-called Landau-Zener transitions. Thus, high-fidelity shuttling should be

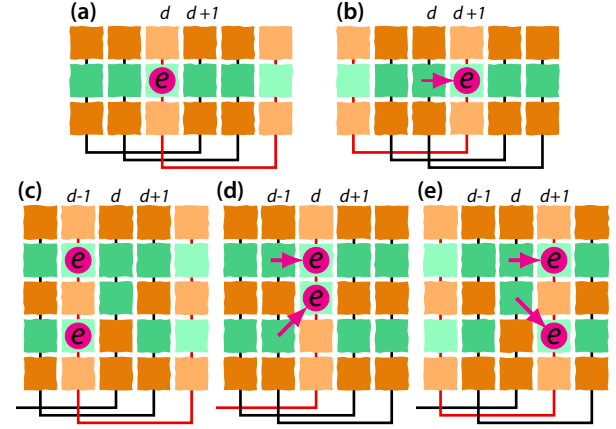


Figure S1. **Programmable pixelgrid.** A dense quantum dot array provides a reconfigurable implementation of the pipeline. Squares, or pixels, represent quantum dot defining metal gates. The decomposition of the algorithm to single-, and two-qubit gates determines which gates acts as plungers (green) and which as barriers (orange). (a)-(b) Shuttling forward along the pixelgrid is implemented with three-stage shuttling. (c)-(e) Two-qubit interactions between pipes are implemented with diagonal shuttling.

performed adiabatically with respect to inter-dot charge transition tunnel rates, and using ramp rates which are not resonant with valley-orbit transitions.

For a simple ballpark figure of adiabaticity, we may estimate probability for charge state error by evaluating the first-order, or single-passage, Landau-Zener transition probability, which is given by $P_{LZ} = \exp(-2\pi\delta)$, where $\delta = t_{ij}^2/(4\nu)$, and furthermore $\nu = A\hbar\omega$ is the approximate drive velocity for a ramp with amplitude A (in units of energy) and angular frequency ω [3]. Over a typical voltage range across an inter-dot-charge transition, $A = e\alpha \times 25$ mV, where $\alpha = 0.1$ is a typical lever arm. At tunnel coupling $t_{ij}/h = 20$ GHz, the ramp can be performed adiabatically ($P_{LZ} < 10^{-4}$) with shuttling times of 9.1 ns or more (corresponding to $\omega/(2\pi) \lesssim 110$ MHz).

b. Control line footprints

A bias tee where current is not expected to flow can be realised using a resistor and a capacitor. Assuming a sheet resistance of $\rho = 100 \Omega/\text{square}$ [4], the footprint of a single $R_{\text{tee}} = 10$ k Ω resistor would be $50 \text{ nm} \times 5 \mu\text{m}$. Like-

* ucapsmp@ucl.ac.uk

wise, assuming a capacitance per area of $1 \text{ pF}/\mu\text{m}^2$ [5], a $C = 159 \text{ pF}$ capacitor, to hit an RC -constant cut-off frequency of $f_{\text{cutoff}} = 100 \text{ kHz}$, would take around $159 \mu\text{m}^2 \approx 12.6 \mu\text{m} \times 12.6 \mu\text{m}$. For a single column of 50 qubits, bias tees could be fitted into an area of approximately $630 \mu\text{m} \times 12.7 \mu\text{m}$. The 1-to- N power splitter can be realised as e.g. a common-source N -parallel-MOSFET.

3. Electric field dependence on applied gate voltages

For the g -factor Stark shift

$$\delta g_q(V_j) = \frac{\partial g}{\partial E_i} \frac{\partial E_i}{\partial V_j} dV_j, \quad (\text{S1})$$

where E_i are the electric field components and V_j the associated gate voltages, we have a corresponding change in electrochemical potential of

$$d\mu_q = -e \sum_j \alpha_{qj} dV_j, \quad (\text{S2})$$

where α_{qj} is the lever arm from dot q to gate j . The change in μ_q would be detrimental to the shuttling scheme when uncompensated, which can be illustrated with the triple QD stability diagrams, shown in main text Figs. 3 (e)-(g). Stability diagrams show the boundaries of regions of constant charge as a function of two (or more, in higher-dimensional graphs) gate voltages. In a successful shuttling sequence, the shuttling waveform takes the electron from the charge configuration $(n_{q+1} n_q n_{q-1}) = (001)$, to (010) , and to (100) , as illustrated in Fig. 3 (e). Uncompensated g -factor modulation using V_q can lead to a change in the proximal ground state charge configurations, which under globally applied shuttling sequence would lead to an error in the charge state as illustrated in Fig. 3 (f).

To estimate the relative contributions of the plunger gate and the μ -compensating gate, we solve for the derivatives $\partial E_i / \partial V$ as follows. We model a metal gate as a rectangular infinitely thin charge sheet centered at origin. The sheet has width a , length b , and a uniform charge density σ . The electric field components can be expressed as the double integrals of Eqs. (S3)-(S5), where $k_e = 1/(4\pi\epsilon_0\epsilon_r)$. These can be computed with Mathematica [6], or by hand using substitutions, which for the second integral of (S5) would read: $x'' = x - x'$, where $dx'' = dx'$, followed by the trigonometric substitution $x''/z = \tan(\theta)$, with $dx'' = d\theta \cos(\theta)^{-2}$. The substitution allows to simplify the integrand in a form which is integrable using trigonometric identities. The resulting functions can be expressed in terms of elementary functions.

Once we fix a heterostructure of planar dielectrics with large surface areas, we obtain a relationship between applied gate voltage V and the effective charge density σ ,

Variable	Symbol	Value	Unit
QD length along x	w_x	50	nm
QD length along y	w_y	50	nm
Si/SiO ₂ oxide thickness	d_{ox}	5	nm
Gate to gate distance	$\Delta\mu_q$	40	nm
Si substrate thickness	d_{SiSub}	0.5	mm
Si dielectric constant	ϵ_{Si}	11.8	
SiO ₂ dielectric constant	ϵ_{ox}	3.8	

Table I. Simulation parameters for the electric field gradient simulations.

as

$$V = - \sum_i \int_{z_i}^{z_{i+1}} d\mathbf{l} \cdot \mathbf{E}(x, y, z), \quad (\text{S6})$$

where the sum is taken over the interfaces between different materials from the charge sheet to the ground plane. For example, there is a single layer of dielectric and substrate between the gate and the ground plane in a planar MOS structure such that $z_0 = 0$, $z_1 = d_{\text{ox}}$, and $z_2 = d_{\text{ox}} + d_{\text{SiSub}}$, where d_{ox} and d_{SiSub} are widths of the dielectric and the Si substrate, respectively. For a path perpendicular to the interfaces $d\mathbf{l} \cdot \mathbf{E} = dz E_z$. The result is a linear relationship

$$\sigma = \sigma(V) = a_\sigma V, \quad (\text{S7})$$

where a_σ is a constant with respect to the coordinates, and is a function of the geometry. The relation (S7) allows us to express $\mathbf{E}(\sigma) = \mathbf{E}(\sigma(V))$, which allows us to evaluate the derivatives $\partial E_i / \partial V$ analytically. Since $\mathbf{E} \propto \sigma \propto V$, $\partial E_i / \partial V \propto \mathbf{E}$, and $\partial E_i / \partial V$ is independent of V . Table I summarises the parameters used in this simulation.

For planar MOS or mostly \pm z-valley-lying wavefunctions, the effect of E_z due to V_q dominates. This is because $\partial E_x / \partial V_q \approx 0.010 \partial E_z / \partial V_q$, $\partial E_x / \partial V_\mu \approx 0.062 \partial E_z / \partial V_q$, and $\partial E_z / \partial V_\mu \approx 0.0037 \partial E_z / \partial V_q$ at site q (see Fig. 3 (g)). We also expect $\partial g / \partial E_z \gg \partial g / \partial E_x$. More generally, when both gates Stark shift the g -factor, compensation is possible, as long as the effects of the gates to g -tuning and μ_q are asymmetric. Then Eq. (S1) simplifies to $\delta g_q(V) \approx (\partial g / \partial E_z) (\partial E_z / \partial V_q) dV_q$.

As discussed in the main text, tuneability of $\delta_{g\pi} = \pm 3.6 \times 10^{-5}$ may require plunger gate voltage shifts of $dV_q = \pm 0.022 \text{ V}$, which can be compensated with $dV_\mu \approx -\alpha_{q\mu} / \alpha_{q\mu} dV_q$. In addition, perfect compensation requires $\alpha_{q\mu} / \alpha_{q\pm 1 q} = \alpha_{q\mu} / \alpha_{q\pm 1 \mu}$, where $\alpha_{q\pm 1 q}$ and $\alpha_{q\pm 1 \mu}$ are the lever arms to of the subsequent and prior QDs to the plunger gate of q and the μ -compensating gate, respectively. The stability diagrams in Fig. 3 (e) are in fact simulated using the μ -compensation scheme described above. The results are identical to those in the absence of g -factor tuning. The stability diagram is sim-

$$E_x = k_e \sigma \int_{-a/2}^{a/2} dx' (x - x') \int_{-b/2}^{b/2} dy' [(x - x')^2 + (y - y')^2 + z^2]^{-3/2}, \quad (\text{S3})$$

$$E_y = k_e \sigma \int_{-a/2}^{a/2} dx' \int_{-b/2}^{b/2} dy' (y - y') [(x - x')^2 + (y - y')^2 + z^2]^{-3/2}, \quad (\text{S4})$$

$$E_z = k_e \sigma z \int_{-a/2}^{a/2} dx' \int_{-b/2}^{b/2} dy' [(x - x')^2 + (y - y')^2 + z^2]^{-3/2}, \quad (\text{S5})$$

ulated from the ground state energy of the electrostatic Hamiltonian. See e.g. [7] for details of the simulation.

4. Nearest-neighbour exchange

a. Nearest-neighbour Hamiltonian

The two-site (for sites i, j), one-orbital Fermi-Hubbard Hamiltonian is block-diagonalised using a second order Schrieffer-Wolff transformation, separating $(1, 1)$ as low-energy states compared to $(2, 0)$ and $(0, 2)$ states [8]. The resulting block-diagonalised Hamiltonian for the $(1, 1)$ subspace, in the basis $\{|\uparrow_i \uparrow_j\rangle, |\uparrow_i \downarrow_j\rangle, |\downarrow_i \uparrow_j\rangle, |\downarrow_i \downarrow_j\rangle\}$, reads

$$H_{2Q} = \begin{pmatrix} (\Delta E_Z + E_Z) & 0 & 0 & 0 \\ 0 & (-\Delta E_Z + J_{--} + J_{--}) & J_{ij} & 0 \\ 0 & J_{ij} & (\Delta E_Z + J_{++} + J_{++}) & 0 \\ 0 & 0 & 0 & (-\Delta E_Z - E_Z) \end{pmatrix}. \quad (\text{S8})$$

Here, $E_Z = E_{Zi}$ is the Zeeman energy of QD i , which defines the Zeeman energy difference $\Delta E_Z = E_{Zj} - E_{Zi}$, and $\epsilon = \epsilon_j - \epsilon_i$ is detuning. Furthermore, we have defined

$$J_{s_1 s_2 s_3}(\epsilon, \Delta E_Z) = \frac{t_{ij}^2}{s_1 \Delta E_Z + s_2 \Delta K + s_3 \epsilon}, \quad (\text{S9})$$

where $s_k \in \{-1, +1\}$, and the exchange strength can be written, as

$$J_{ij}(\epsilon, \Delta E_Z) = \frac{1}{2} (J_{+++} + J_{++-} + J_{-++} + J_{-+-}) \quad (\text{S10})$$

$$\begin{aligned} &\approx \frac{t^2}{\Delta K + \epsilon} + \frac{t^2}{\Delta K - \epsilon}, \\ &= \frac{2t^2 \Delta K}{\Delta K^2 - \epsilon^2}. \end{aligned} \quad (\text{S11})$$

We note that $J_{ij} \geq 0$. Equation (S11) holds when $\Delta E_Z \ll \Delta K$. We also define short-hands for the diagonal exchange-like elements

$$J_i = -J_{---} - J_{--+} \quad (\text{S12})$$

$$J_j = -J_{++-} - J_{-+-}. \quad (\text{S13})$$

b. Native two-qubit unitary operation

The exact unitary time evolution that $H_{2Q}(\epsilon)$ (S8) generates, which is our native two-qubit interaction, is given by

$$\begin{aligned} U_{\text{Nat}}(\epsilon) &= \exp(-iH_{2Q}t/\hbar) \\ &= \left\{ e^{-i(E_Z + \Delta E_Z)t/\hbar + iJ_{ij}t/\hbar} |\uparrow_i \uparrow_j\rangle\langle\uparrow_i \uparrow_j| + \right. \\ &\quad \left[\cos(\Omega_{ij}t) + \frac{i\Delta_{ij}}{\Omega_{ij}} \sin(\Omega_{ij}t) \right] |\uparrow_i \downarrow_j\rangle\langle\uparrow_i \downarrow_j| + \\ &\quad \frac{iJ_{ij}}{\Omega_{ij}} \sin(\Omega_{ij}t) (|\uparrow_i \downarrow_j\rangle\langle\downarrow_i \uparrow_j| + |\downarrow_i \uparrow_j\rangle\langle\uparrow_i \downarrow_j|) + \\ &\quad \left[\cos(\Omega_{ij}t) - \frac{i\Delta_{ij}}{\Omega_{ij}} \sin(\Omega_{ij}t) \right] |\downarrow_i \uparrow_j\rangle\langle\downarrow_i \uparrow_j| + \\ &\quad \left. e^{i(E_Z + \Delta E_Z)t/\hbar + iJ_{ij}t/\hbar} |\downarrow_i \downarrow_j\rangle\langle\downarrow_i \downarrow_j| \right\} e^{-iJ_{ij}t/\hbar}. \end{aligned} \quad (\text{S14})$$

Here,

$$\Delta_{ij} := \Delta E_Z + (J_i - J_j)/2 \quad (\text{S15})$$

$$\hbar\Omega_{ij}(\Delta E_Z, J_{ij}) := \sqrt{\Delta_{ij}^2 + J_{ij}^2}. \quad (\text{S16})$$

To analyse the dynamics further, we may parameterise $U_{\text{Nat}}(\epsilon)$, as

$$U_{\text{Nat}}(\epsilon, \phi, \chi) = e^{i\phi \cos(\chi)} \times \begin{pmatrix} e^{-i\phi_Z - i\phi \cos(\chi)} & 0 & 0 & 0 \\ 0 & [\cos(\phi) + i\sin(\chi)\sin(\phi)] & -i\cos(\chi)\sin(\phi) & 0 \\ 0 & -i\cos(\chi)\sin(\phi) & [\cos(\phi) - i\sin(\chi)\sin(\phi)] & 0 \\ 0 & 0 & 0 & e^{i\phi_Z - i\phi \cos(\chi)} \end{pmatrix}. \quad (\text{S17})$$

Here, we have defined the parameters

$$\chi := \arctan(x) \quad (\text{S18})$$

$$x(\Delta E_Z, J_{ij}) := \frac{\Delta_{ij}}{J_{ij}} \quad (\text{S19})$$

$$\phi(t, \Delta E_Z, J_{ij}) := \frac{t}{\Omega_{ij}}. \quad (\text{S20})$$

Figure S2 visualises the conversion between x and χ . Notice that the x -axis scale is not linear.

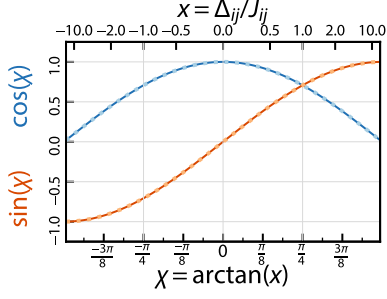


Figure S2. **Attainable rotation angles.** Illustration of the required ratio $x = \Delta_{ij}/J_{ij}$ corresponding to the sine (orange trace) and cosine (blue trace) of particular rotation angles χ .

5. Two-qubit gates

We define a few well-known two-qubit gates for reference [9]. From the family of SWAP-rotation gates,

$$\text{SWAP} \triangleq \begin{pmatrix} 1 & 0 & 0 & 0 \\ 0 & 0 & 1 & 0 \\ 0 & 1 & 0 & 0 \\ 0 & 0 & 0 & 1 \end{pmatrix} \quad (\text{S21})$$

$$\sqrt{\text{SWAP}} \triangleq \begin{pmatrix} 1 & 0 & 0 & 0 \\ 0 & \frac{1+i}{2} & \frac{1-i}{2} & 0 \\ 0 & \frac{1-i}{2} & \frac{1+i}{2} & 0 \\ 0 & 0 & 0 & 1 \end{pmatrix} \quad (\text{S22})$$

$$\text{SWAP}(\theta) \triangleq \begin{pmatrix} e^{i\theta} & 0 & 0 & 0 \\ 0 & \cos(\theta) & i \sin(\theta) & 0 \\ 0 & i \sin(\theta) & \cos(\theta) & 0 \\ 0 & 0 & 0 & e^{i\theta} \end{pmatrix}. \quad (\text{S23})$$

The so-called Givens rotation gate has a similar form to the SWAP-rotation gate in the $m_z = 0$ subspace:

$$\text{Givens}(\phi) \triangleq \begin{pmatrix} 1 & 0 & 0 & 0 \\ 0 & \sin(\phi) & -\cos(\phi) & 0 \\ 0 & \cos(\phi) & \sin(\phi) & 0 \\ 0 & 0 & 0 & 1 \end{pmatrix}. \quad (\text{S24})$$

We define the phase gates

$$\text{CPhase}(\phi) \triangleq \begin{pmatrix} 1 & 0 & 0 & 0 \\ 0 & 1 & 0 & 0 \\ 0 & 0 & 1 & 0 \\ 0 & 0 & 0 & e^{i\phi} \end{pmatrix} \quad (\text{S25})$$

$$\text{Ising}(\phi) \triangleq \begin{pmatrix} 1 & 0 & 0 & 0 \\ 0 & e^{i\phi} & 0 & 0 \\ 0 & 0 & e^{i\phi} & 0 \\ 0 & 0 & 0 & 1 \end{pmatrix}. \quad (\text{S26})$$

6. Engineering the native operation

Here, we show an example protocol for choosing the exchange strength such, that the resulting unitary time evolution corresponds to the desired two-qubit gate.

In preconfiguration, the gate time τ_{2Q} , operation (CPhase, Ising, or Givens-like), and rotation angle (either α or χ) are set. In addition, the site-dependent g -factors G_{qi} and G_{qj} are known, as well as the detuning ϵ , and external dc magnetic field B_0 .

As discussed in the main text, the operation determines φ such, that for the phase gates we take $\varphi = \pi + 2\pi n$ for some n , and for the Givens-like gate we take $\varphi = \pi/2 + 2\pi n$. Initially, we assume, that $n = 0$. We then solve for the desired x based on the gate rotation angle, i.e. either α or χ . For the phase gates

$$\alpha = \begin{cases} \frac{\pi + 2\pi n}{\sqrt{1+x^2}} + \pi & \text{for Ising} \\ 2 \frac{\pi + 2\pi n}{\sqrt{1+x^2}} & \text{for CPhase.} \end{cases} \quad (\text{S27})$$

For the CPhase gate, we take

$$n = \text{ceil}(\varphi/\alpha) + 1 \\ |x| = \frac{\sqrt{(2\varphi)^2 - \alpha^2}}{\sqrt{\alpha^2}}.$$

For the Ising gate, we take

$$n = \text{ceil}(|\varphi|/|\alpha - \pi|) + 1 \\ k = \text{floor}(n/2) \\ |x| = \frac{\sqrt{\varphi^2 - [(2k-1)\pi + \alpha]^2}}{(2k-1)\pi + \alpha}.$$

For the Givens-like gate, $|x| = \tan(\chi)$ and $n = 0$. The sign of x is determined based on ΔE_Z ($J_{ij} \geq 0$). These solutions are not unique. We also note that care must be taken if the desired rotation angle $\alpha = 0$ or $\alpha = 2\pi$ for the CPhase gate, when $\alpha = \pi$ for the Ising gate.

The solved x translates to exchange strength J_{ij} (and Δ_{ij}) via t_{ij} , and furthermore to Ω_{ij} . Since Ω_{ij} and φ are fixed, in general, the gate time $\tau = \varphi/\Omega_{ij}$ is shorter compared to the target τ_{2Q} . We use the above solutions for $|x|$ at increasing n until $\tau \geq \tau_{2Q}$, to find the n for which τ is closest to τ_{2Q} . For a high-fidelity operation, we require higher accuracy in τ than what choosing n can provide. To this end, we may fine-tune τ using g -factor tuning with either of the qubits, to minimize the gate time error

$$\delta\tau = \left| \tau_{2Q} - \frac{\varphi}{\sqrt{[x^{-1}\Delta E_Z(\delta g)]^2 + \Delta E_Z(\delta g)^2 \hbar^{-1}}} \right|. \quad (\text{S28})$$

At the best value of δg , we re-evaluate the required t_{ij} to hit the desired J_{ij} , and hence x and Ω_{ij} .

7. Semiclassical Rabi model

The dynamics of a qubit with Larmor frequency ω_0 , coupling to a transversal magnetic field mode of frequency ν and amplitude B_1 , leading to coupling strength

$g^* \mu_B B_1 / \hbar = \omega_1$, is described by the semiclassical Rabi model, which we display for convenience. The Hamiltonian reads

$$\begin{aligned} H_{1Q} &= \frac{1}{2} \hbar \omega_0 \sigma_z + \frac{1}{2} \hbar \omega_1 (\sigma_+ e^{-i\nu t + i\varphi} + \sigma_- e^{i\nu t - i\varphi}) \\ &= \frac{1}{2} \hbar \omega_0 \sigma_z + \frac{1}{2} \hbar \omega_1 \left\{ \sigma_x \cos[\nu t + \varphi] + \sigma_y \sin[\nu t + \varphi] \right\}, \end{aligned} \quad (\text{S29})$$

where $\varphi = \phi + \phi_\alpha$.

In a frame rotating by $H_R = e^{-i\omega_R t}$ the semiclassical Rabi Hamiltonian (S29) retains its form, but the frequencies get replaced, as $\omega_0 \rightarrow \Delta_0 = \omega_0 - \omega_R$, $\nu \rightarrow \Delta_\nu = \nu - \omega_R$.

The time evolution generated by this Hamiltonian reads

$$\begin{aligned} U_{1Q}(t, \Delta, \nu) &= \exp(-iH_{1Q}t/\hbar) \\ &= \frac{e^{i\nu t/2}}{2\Omega} \left\{ e^{-i\Omega t/2} [\Omega - \Delta] + e^{i\Omega t/2} [\Omega + \Delta] \right\} |g\rangle\langle g| \\ &\quad - \frac{i\omega_1}{\Omega} e^{i\nu t/2 + i\varphi} \sin(\Omega t/2) |g\rangle\langle e| \\ &\quad - \frac{i\omega_1}{\Omega} e^{-i\nu t/2 - i\varphi} \sin(\Omega t/2) |e\rangle\langle g| \\ &\quad + \frac{e^{-i\nu t/2}}{2\Omega} \left\{ e^{-i\Omega t/2} [\Omega + \Delta] + e^{i\Omega t/2} [\Omega - \Delta] \right\} |e\rangle\langle e|, \end{aligned} \quad (\text{S30})$$

where $\Omega = \sqrt{\Delta^2 + \omega_1^2}$ is the Rabi frequency, and $\Delta = \omega_0 - \nu$ is the qubit-field detuning. At resonance $\nu = \omega_0$, $\Delta = 0$ and $\Omega = \omega_1$. We may also write the operator in terms of Pauli matrices, as

$$\begin{aligned} U_{1Q}(t, \Delta, \nu) &= [\cos(\Omega t/2) \cos(\nu t/2) - \frac{\Delta}{\Omega} \sin(\Omega t/2) \sin(\nu t/2)] \mathbf{I} \\ &\quad - i [\cos(\Omega t/2) \sin(\nu t/2) + \frac{\Delta}{\Omega} \sin(\Omega t/2) \cos(\nu t/2)] \sigma_z \\ &\quad + \frac{i\omega_1}{\Omega} \sin(\Omega t/2) [\cos(\varphi + \nu t/2) \sigma_x + \sin(\varphi + \nu t/2) \sigma_y]. \end{aligned} \quad (\text{S31})$$

At resonance $\nu = \omega_0$, $\Delta = 0$ and $\Omega = \omega_1$. Then,

$$\begin{aligned} U_{1Q}(t, \Delta = 0, \nu) &= \cos(\omega_1 t/2) \cos(\nu t/2) \mathbf{I} - i \cos(\omega_1 t/2) \sin(\nu t/2) \sigma_z \\ &\quad + i \sin(\omega_1 t/2) [\cos(\varphi + \nu t/2) \sigma_x + \sin(\varphi + \nu t/2) \sigma_y]. \end{aligned} \quad (\text{S32})$$

In the frame $\nu = 0$, the resonant unitary operator

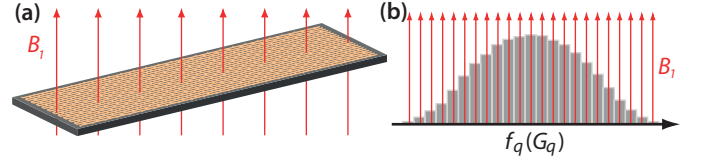


Figure S3. **Global \sqrt{X} gate.** (a) In the nanogrid, we apply transversal single-qubit control (represented as red vertical arrows) chip-globally using e.g. dielectric or superconducting resonators. (b) Qubits with a Larmor frequency distribution, represented as a gray histogram, can be driven with evenly spaced B_1 tones, or bins (red vertical arrows). Using bin spacing determined by g -factor tuneability, $g_{\text{bin}} = 2\delta g_\pi$, all qubits can be tuned to their closest bins.

(Eq. (S32)) reduces to

$$\begin{aligned} U_{1Q}(t, \Delta = 0, \nu = 0) &= \cos(\omega_1 t/2) \mathbf{I} - i \sin(\omega_1 t/2) [e^{i\varphi} \sigma_- + e^{-i\varphi} \sigma_+], \\ &= \cos(\omega_1 t/2) \mathbf{I} - i \sin(\omega_1 t/2) [\cos(\varphi) \sigma_x + \sin(\varphi) \sigma_y]. \end{aligned} \quad (\text{S33})$$

The time evolution Eq. (S33) realises \sqrt{X} up to a global phase, as

$$\begin{aligned} U_{1Q}[t = \pi/(2\omega_1); \Delta = 0; \nu_i = 0] &= X(\pi/2) \\ &= e^{-i\pi/4} \sqrt{X}. \end{aligned} \quad (\text{S34})$$

Here, $X(\theta) = e^{-i\theta\sigma_x/2}$.

8. Multitone driving with frequency binning

In the main text we discuss global transversal control (see Fig. S3 (a) for illustration). The difficulty with single-tone driving is illustrated by the Bloch-sphere polar angle $\arccos(\Delta_{q\nu}/\Omega_q(t))$, where $\Delta_{q\nu} = \omega_{0q} - \nu$ is the qubit-drive frequency detuning, and $\Omega_q(t) = \sqrt{\Delta_{q\nu}^2 + \omega_{1q}^2(t)}/\hbar$ is the time-dependent Rabi frequency. At small detuning $\Delta_{q\nu} \ll \omega_{1q}(t)$, $\arccos(\Delta_{q\nu}/\Omega_q) \approx \pi/2$ and the effective magnetic field axis is on the transversal plane for all qubits, whereas for $\Delta_{q\nu} \gg \omega_{1q}(t)$ the effective field axis is significantly qubit-dependent. The small-detuning limit holds when $G_q/g_{\text{Si}} \ll B_1(t)/B_0$. At $B_0 = 1$ T, to reach e.g. $G_q/g_{\text{Si}} = 0.05 B_1/B_0$ with $G_q \leq 10^{-2}$, we would require $B_1 = 100$ mT, which is technologically out of reach. The minimum amplitude required to bring a qubit with $G_q = 10^{-2}$ from the Bloch sphere north or south pole onto the transversal plane requires $B_1 = 5$ mT (coinciding with $\Delta_{q\nu} = \omega_{1q}(t)$). Even this is technologically challenging.

While insensitivity to qubit frequencies can be increased with pulse shaping close to the small-detuning limit [10], far from the small-detuning limit, we propose instead to achieve global control using frequency binning [11], which is illustrated in Fig. S3 (b). That is, we

employ a control pulse of length τ_{1Q} consisting of $2N_1$ drive tones, at

$$\nu_i = [g_{Si} + ig_{\text{bin}}]\mu_B B_0/\hbar \quad (\text{S35})$$

where $i = 0 \pm 1, 2, 3, \dots, N_1$ is the bin, and the bin width is determined by the g -factor tuneability according to $g_{\text{bin}} = 2\delta g_\pi$, i.e. a bin width of $\nu_{i+1} - \nu_i = 2$ MHz. The drive is akin to a finite-component frequency comb. Then, using the g -factor tuning described above, the frequency of each qubit may be tuned into resonance with the closest bin. We expect this bin width to be significantly larger than intrinsic ESR linewidths of $\mathcal{O}(1 \text{ kHz})$ [12]. For example, choosing $N_1 = 140$ covers a g -factor distribution with $G_q \leq \pm 10^{-2}$.

There is also less power dissipation with frequency binning compared to single-tone driving due to the much smaller required amplitudes. At $B_0 = 1 \text{ T}$, $B_{1i} \approx 35.7 \mu\text{T}$ yields $\tau_{1Q} = 1 \mu\text{s}$. The dissipated power scales as $P = a|B_1|^2$ for a constant a , such that $aN|B_{1i}|^2 = 280 \times |35.7 \times 10^{-6}|^2 \ll |B_1|^2$ for $B_1 = 5 \text{ mT}$.

The effect of a single classical drive tone on a qubit is described by the unitary time evolution generated by the semiclassical Rabi model (see Supplementary Sec. S7) $U_{1Q}(t, \Delta_{qv}, \nu)$. While frequency binning allows one to drive all qubits resonantly ($\omega_{0q} = \nu_i$ for all q for some i), viewing the dynamics from a global frame, the laboratory frame is not resonant with any of the drive tones. In the laboratory frame, qubit dynamics is described by

$$U_{1Q}[t = \pi/(2\omega_1); \Delta = 0; \nu_i] = Z(\varphi_i)X(\pi/2) \quad (\text{S36})$$

for some φ_i which increases with i . This can be shown, as

$$\begin{aligned} Z(\theta)U_{1Q}(\Delta = 0, \nu = 0) &= \cos(\omega_1 t/2) \cos(\theta) \mathbf{I} - i \cos(\omega_1 t/2) \sin(\theta) \sigma_z \\ &\quad - i \sin(\omega_1 t/2) [\cos(\varphi + \theta) \sigma_x + \sin(\varphi + \theta) \sigma_y]. \end{aligned} \quad (\text{S37})$$

Then, $Z(\theta)U_{1Q}(t, \Delta = 0, \nu = 0) = U_{1Q}(t, \Delta = 0, \nu)$ with $\theta = \nu t$. This Z -rotation can be absorbed into $Z(\varphi_q)$.

In Fig. S4, we visualise gate operations using the decomposition to a rotation direction (n_x, n_y, n_z) ($n_k \in [-1, 1]$), which is a vector on the Bloch sphere, and the rotation angle $\theta \in [-\pi, \pi]$. The decomposition allows us to study the conformity of U_{1Q} to the $Z(\varphi_i)X(\pi/2)$ operation. The ideal gate $X(\pi/2)$ has a decomposition with $\theta = \pi/2$, $n_x = -1$, $n_y = n_z = 0$. In comparison, $Z(\varphi_i)X(\pi/2)$ has a linearly decreasing n_y and n_z for linearly increasing φ_i , and thus a small quadratic deviation from $\theta = \pi/2$ and $n_x = -1$ with increasing bin number.

We study the gate fidelity of the analytical semiclassical Rabi unitary U_{1Q} as the conformity to $Z(\varphi_i)X(\pi/2)$ under noise. Unless otherwise stated, we use the same parameters as in the simulations described in main text. In particular, we take $B_{1i} \approx 35.7 \mu\text{T}$ (linearly decreasing with increasing bin number), $g_{\text{bin}} = 2\delta g_\pi$. The fidelities are essentially bin-independent, since the dominant errors come from the frequency at f_{Si} . For a fixed bin

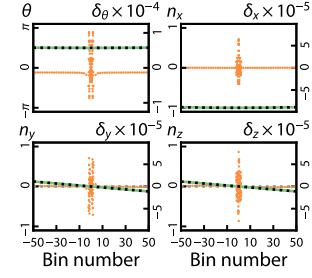


Figure S4. Bin-dependence of the column-global single-qubit operation. Gate decomposition coefficients θ , n_x , n_y , and n_z as a function of even bin numbers. Light gray and dark gray dotted lines show the decomposition of ideal $X(\pi/2) = e^{i\pi/4}\sqrt{X}$ and $Z(\varphi_i)X(\pi/2)$ for linearly increasing φ_i , respectively. Solid green line shows the decomposition of the analytical semiclassical Rabi unitary operator with drive tone ν_i , and numerically integrated time evolution under the semiclassical Rabi Hamiltonian, U_{1Q} , with a single drive tone at ν_i , corresponding to the resonant bin. Orange datapoints show the decomposition differences δ_θ , δ_x , δ_y , and δ_z between U_{1Q} with a single drive tone, and five drive tones from ν_{i-2} to ν_{i+2} and a smaller ω_1 . The Hamiltonian natively coincides with $X(\pi/2)$ (viewed from the frame rotating with the average g -factor Larmor frequency f_{Si}) at resonance $\omega_0 = \nu$, for qubit Larmor frequency ω_0 , and drive tone ν , in the reference frame $\nu = 0$ (see the overlap point between the light gray and the blue traces). At reference frames with $\nu \neq 0$, resonantly driven qubit dynamics coincide with $Z(\varphi_i)X(\pi/2)$ instead (see the overlap between the dark gray and the green traces). Effects of cross-talk can be compensated with a globally reduced B_1 amplitude and thus ω_1 , while retaining a fixed τ_{1Q} (overlapping solid lines). drive tones ν_i , and ν_{i-1} , ν_i , and ν_{i+1} for each bin (agreement is better than $1 - 10^{-4}$ for all bins).

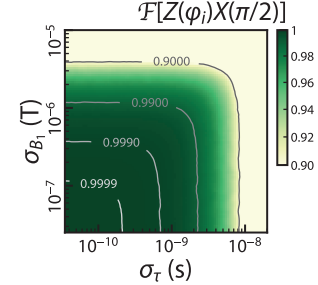


Figure S5. Global \sqrt{X} gate fidelity. Process fidelity of $Z(\varphi_i)X(\pi/2)$ with $Z(\varphi_i)$ determined by the bin (here, $i = 10$), as a function of variance in gate time σ_τ , and in the magnetic field component σ_{B_1} .

$i = 10$, we plot the $Z(\varphi_i)X(\pi/2)$ fidelity as a function of gate time error σ_τ , and noise in the magnetic field component σ_{B_1} , in Fig. S5. Fidelity behaves similarly to the Z -rotation gate fidelity, with noise sources contributing individually.

9. Variational quantum eigensolvers

The pipeline can act as the dedicated spin-qubit hardware for the NISQ variational quantum eigensolver (VQE) algorithm of Ref. [13]. We thus provide the relationship between the pipeline hardware layout and the VQE application in Ref. [13].

VQEs try to find the ground state of a problem Hamiltonian $H : \mathcal{H} \rightarrow \mathcal{H}$ acting on Hilbert space \mathcal{H} using a circuit that prepares a representation of a Hilbert space state $|\psi(\theta_k)\rangle \in \mathcal{H}$, and measures the expectation value $\langle \psi(\theta_k) | H | \psi(\theta_k) \rangle$. The state with the smallest expectation value thus provides a best estimate for the ground state energy. The parameters θ_k are varied between runs $k = 1, \dots, N_r$ by varying rotation angles of quantum gates in the circuit. For example, using the so-called Jordan-Wigner mapping, the qubit logical 0 and 1 correspond to occupancies of 0 and 1 of specific site s and spin σ , i.e. fermionic Fock states $|0_{s\sigma}\rangle$ and $|1_{s\sigma}\rangle = c_{s\sigma}^\dagger |0\rangle$. In this way, a coherent 50-qubit logical state may represent the coherent superposition of Fock states of 5×5 fermionic sites.

A single run of VQE generally consists of four stages: (i) qubit-string state initialisation; (ii) state evolution into a classically solvable Hilbert-space-state; (iii) state evolution into (generally) non-classically-tractable Hilbert-space-state; (iv) as many measurements of observables corresponding to mutually commuting operators, proportional to terms required to measure entire state expectation values of problem Hamiltonian summands (which, summed up, sum to the energy expectation value), as possible. The minimum number of runs with fixed parameters for a single estimation of $\langle \psi(\theta_k) | H | \psi(\theta_k) \rangle$ thus depends on the details of how the problem Hamiltonian summands decompose to commuting (which can be measured during a single run) and

non-commuting (requiring different runs) quantum logic gates.

Stage (iii) contains the variational optimisation, while stage (ii) has fixed-parameter circuit decompositions depending on the classically tractable state of choice. In the so-called Hamiltonian ansatz, stage (iii) consists of a series of blocks of quantum logic gates, each block representing Trotterised time evolution of the Hilbert-space-state, as

$$\prod_{n=1}^{N_H} e^{-i\theta_{nk}h_n} \approx \prod_{n=1}^{N_H} (1 - i\theta_{nk}h_n), \quad (\text{S38})$$

where the underlying problem Hamiltonian (such as the 5×5 Fermi-Hubbard Hamiltonian) is the sum

$$H = \sum_{n=1}^{N_H} \lambda_n h_n \quad (\text{S39})$$

with operators $h_n : \mathcal{H} \rightarrow \mathcal{H}$. For the Fermi-Hubbard model, the h_n are the on-site repulsion operators, and the hopping operators. Each h_n has fixed gate representations, based on the gate representations of the fermionic operators themselves. The application of the series of these blocks then allows to represent the adiabatic switching on of the on-site repulsion in the simulated model, for example. Details of gate decompositions for each stage can be found from Ref. [13]. In terms of the hardware implementation, the key results are that all circuits in stages (ii) and (iii) decompose into $Z_i(\varphi_{ik})$ and $\text{SWAP}_{ij}(\varphi_{ijk})$, laid out in time steps with single- and two-qubit gates alternating in roughly equal numbers, with the two-qubit gates 'weaving' the different qubit states. Stages (i) and (iv) also require stages of $X_i(\varphi_{ik})$ and $Y_i(\varphi_{ik})$ for the qubit-flips in (i), and for the measurement of observables of mutually commuting operators in (iv).

-
- [1] Ha, W.; Ha, S. D.; Choi, M. D.; Tang, Y.; Schmitz, A. E.; Levendordf, M. P.; Lee, K.; Chappell, J. M.; Adams, T. S.; Hulbert, D. R., et al. **A flexible design platform for Si/SiGe exchange-only qubits with low disorder**. *Nano Letters* **2021**, *22*, 1443–1448.
 - [2] Weinstein, A. J.; Reed, M. D.; Jones, A. M.; Andrews, R. W.; Barnes, D.; Blumoff, J. Z.; Euliss, L. E.; Eng, K.; Fong, B. H.; Ha, S. D., et al. Universal logic with encoded spin qubits in silicon. *Nature* **2023**, *615*, 817–822.
 - [3] Shevchenko, S. N.; Ashhab, S.; Nori, F. Landau–Zener–Stückelberg interferometry. *Physics Reports* **2010**, *492*, 1–30.
 - [4] Jin, X.; Weimer, C.; Zhang, Y.; Schröter, M. **Modeling the temperature dependence of sheet and contact resistances in SiGe: C HBTs from 4.3 to 423 K**. 2020 IEEE BiCMOS and Compound Semiconductor Integrated Circuits and Technology Symposium (BCICTS). 2020; pp 1–4.
 - [5] Boter, J. M.; Dehollain, J. P.; Van Dijk, J. P.; Xu, Y.; Hensgens, T.; Versluis, R.; Naus, H. W.; Clarke, J. S.; Veldhorst, M.; Sebastiano, F., et al. **Spiderweb array: A sparse spin-qubit array**. *Physical Review Applied* **2022**, *18*, 024053.
 - [6] Mathematica 12.1.1.0 is able to integrate the planar components E_x and E_y , and the first integral of E_z . The second integral is evaluated after a transform of variables.
 - [7] Patomäki, S.; Williams, J.; Berritta, F.; Lainé, C.; Fogarty, M.; Leon, R.; Jussot, J.; Kubicek, S.; Chatterjee, A.; Govoreanu, B., et al. **An elongated quantum dot as a distributed charge sensor**. *arXiv preprint arXiv:2301.01650* **2023**,
 - [8] Meunier, T.; Calado, V. E.; Vandersypen, L. M. K. **Efficient controlled-phase gate for single-spin qubits in quantum dots**. *Physical Review B* **2011**, *83*, 121403.
 - [9] Crooks, G. E. **Gates, states, and circuits**. **2020**,

- [10] Hansen, I.; Seedhouse, A. E.; Saraiva, A.; Laucht, A.; Dzurak, A. S.; Yang, C. H. **Pulse engineering of a global field for robust and universal quantum computation.** *Physical Review A* **2021**, *104*, 062415.
- [11] Fogarty, M. A. **Silicon edge-dot architecture for quantum computing with global control and integrated trimming.** *arXiv preprint arXiv:2208.09172* **2022**,
- [12] Veldhorst, M.; Hwang, J. C. C.; Yang, C. H.; Leenstra, A. W.; de Ronde, B.; Dehollain, J. P.; Muhonen, J. T.; Hudson, F. E.; Itoh, K. M.; Morello, A. t. **An addressable quantum dot qubit with fault-tolerant control-fidelity.** *Nature nanotechnology* **2014**, *9*, 981.
- [13] Cai, Z. **Resource Estimation for Quantum Variational Simulations of the Hubbard Model.** *Physical Review Applied* **2020**, *14*, 014059.